

# VLT/ISAAC Spectra of the $H\beta$ Region in Intermediate-Redshift Quasars\*

## III. $H\beta$ Broad Line Profile Analysis and Inferences about BLR Structure

P. Marziani<sup>1</sup>, J. W. Sulentic<sup>2</sup>, G. M. Stirpe<sup>3</sup>, S. Zamfir<sup>2</sup>, and M. Calvani<sup>1</sup>

<sup>1</sup> INAF, Osservatorio Astronomico di Padova, Vicolo dell' Osservatorio 5, 35122 Padova, Italy  
e-mail: paola.marziani@oapd.inaf.it; massimo.calvani@oapd.inaf.it

<sup>2</sup> Department of Physics and Astronomy, University of Alabama, Tuscaloosa, AL 35487, USA  
e-mail: jsulenti@bama.ua.edu, zamfi001@bama.ua.edu

<sup>3</sup> INAF, Osservatorio Astronomico di Bologna, Via Ranzani 1, 40127 Bologna, Italy  
e-mail: giovanna.stirpe@oabo.inaf.it

Received ; accepted

### ABSTRACT

**Aims.** We present new VLT ISAAC spectra for 30 quasars, which we combine with previous data to yield a sample of 53 intermediate redshift ( $z \approx 0.9 - 3.0$ ) sources. The sample is used to explore properties of prominent lines in the  $H\beta$  spectral region of these very luminous quasars.

**Methods.** We compare this data with two large low redshift ( $z < 0.8$ ) samples in a search for trends over almost 6dex in source luminosity.

**Results.** We find two major trends: (1) a systematic increase of minimum FWHM  $H\beta$  with luminosity (discussed in a previous paper). This lower FWHM envelope is best fit assuming that the narrowest sources radiate near the Eddington limit, show line emission from a virialized cloud distribution, and obey a well defined broad line region size vs. luminosity relation. (2) A systematic decrease of equivalent width  $[\text{OIII}]\lambda\lambda 4959, 5007$  (from  $W \approx 15$  to  $\sim 1 \text{ \AA}$ ) with increasing source bolometric luminosity (from  $\log L_{\text{bol}} \approx 43$  to  $\log L_{\text{bol}} \approx 49$ ). Further identified trends require discrimination between so-called Population A and B sources. We generate median composite spectra in six luminosity bins to maximize S/N. Pop. A sources show reasonably symmetric Lorentzian  $H\beta$  profiles at all luminosities while Pop. B sources require two component fits involving an unshifted broad and a redshifted very broad component. Very broad  $H\beta$  increases in strength with increasing  $\log L_{\text{bol}}$  while the broad component remains constant resulting in an apparent ‘‘Baldwin effect’’ with equivalent width decreasing from  $W \sim 80$  to  $\sim 20 \text{ \AA}$  over our sample luminosity range. The roughly constant equivalent width shown by the  $H\beta$  very broad component implies production in optically-thick, photoionized gas. The onset of the redshifted very broad component appears to be a critical change that occurs near the Pop. A-B boundary at  $\text{FWHM } H\beta \approx 4000 \text{ km s}^{-1}$  which we relate to a critical Eddington ratio ( $\approx 0.2 \pm 0.1$ ).

**Key words.** quasars: general quasars: emission lines – emission lines: profiles – black hole physics

## 1. Introduction

Much remains to be defined in quasar research even if one restricts attention to the broad emission lines often used to define them. Their broad line spectra show considerable diversity complicating attempts to generate composite spectra and making estimates of intrinsic properties such as black hole mass unreliable. In addition, the relationship between broad line emitting active galactic nuclei (Type 1 AGN) and various classes of sources that do not show broad lines (e.g. Type 2 AGN, LINERs, Blazars, NLRGs) is still uncertain. It is difficult to imagine how advances in physical understanding can come until source phenomenology is clarified. We have focused on clarifying the phenomenology of Type 1 sources because of their relatively unambiguous broad line signature. Leaving aside reverberation studies making use of source variability, observational advances can be expected to come from two areas of spectroscopic investi-

gation: (1) inter-line comparisons (from  $\text{Ly}\alpha$  to  $\text{H}\alpha$ ) in terms of relative intensity and profile shape (e.g., Shang et al., 2007); (2) moderate dispersion and high S/N studies of the  $H\beta$  spectral region in quasars with  $z \geq 1.0$ . There is a long history of infrared spectroscopy of the Balmer lines in high redshift AGN (e.g., Kuhr et al., 1984; Espey et al., 1989; Carswell et al., 1991; Hill et al., 1993; Baker et al., 1994; Elston et al., 1994; Evans et al., 1998; Murayama et al., 1998, 1999) but only recently has it become possible to obtain spectra with resolution and S/N comparable to those for optical spectra of low  $z$  sources. IR spectroscopy of  $H\beta$  at  $z \geq 1.0$  enables one to use the same line ( $H\beta$ ), the same rest frame determination ( $[\text{OIII}]\lambda\lambda 4959, 5007$  or narrow component of  $H\beta$ ) and the same reduction procedures for estimating the central black hole mass ( $M_{\text{BH}}$ ). Even so observations of the most numerous and most luminous quasars at  $z \approx 2$  can only be made when the optical lines are redshifted into one of the IR bands of high atmospheric transmission.

Spectrographs on HST have provided UV coverage of higher ionization broad lines in low- $z$  Type 1 sources (Seyfert 1 and quasars) with  $\sim 150$  sources having useful measures of

Send offprint requests to: P. Marziani

\*Based on observations made with ESO Telescopes at the Paranal Observatory under programme ID 073.B-0398(A) and 075.B-0171(A).

Civ $\lambda$ 1549 (e.g., Brotherton et al., 1994; Marziani et al., 1996; Baskin & Laor, 2005; Sulentic et al., 2007). Almost all of these sources now have matching optical spectroscopic measures of the  $H\beta$  region (e.g., Marziani et al., 2003a; Baskin & Laor, 2005; Shang et al., 2007). Continuing with a litany of difficulties we note that even some of these UV observations show marginal S/N while many do not cover the full range from Ly $\alpha$  to 3500 Å. Optical coverage is usually not synoptical. This makes detailed intercomparisons of the strongest high and low ionization broad lines possible for only a few tens of objects at best. The lack of spectra covering the rest frame from Ly $\alpha$  to H $\alpha$  is unfortunate since line intensity and profile ratios provide a wealth of physical constraints. The ability to compare lines from ions of widely different ionization potentials has helped to elucidate two main emitting regions within the broad line region (BLR): (a) one responsible for the production of low-ionization lines (LIL) like FeII,  $H\beta$  as well as MgII $\lambda$ 2800 and (b) one that emits mainly lines (Civ $\lambda$ 1549, HeII $\lambda$ 4686) from ions of high ionization potential (HIL; e.g., Collin-Souffrin et al., 1988). Meaningful line profile studies begin with observations of Civ $\lambda$ 1549 and  $H\beta$  as the most typical HIL and LIL.

Our attempt at clarifying type 1 AGN phenomenology involves the Eigenvector 1 formalism of Boroson & Green (1992) and was later expanded into 4 dimensions (4DE1). The latter focused on four parameters including measures of  $H\beta$  and FeII (Sulentic et al., 2000a,b, 2007). Changes in the width and relative strength of  $H\beta$  and FeII lines appear to be primarily related to Eddington ratio convolved with source orientation (Shang et al., 2003; Marziani et al., 2003b; Yip et al., 2004; Boroson, 2005; Collin et al., 2006). 4DE1 studies also introduced the concept of two quasar populations A and B that maximize phenomenological differences and possibly identify sources with higher and lower Eddington ratios respectively. The width of broad  $H\beta$  (FWHM or 2<sup>nd</sup> profile moment  $\sigma$ ) have been widely used as measures of velocity dispersion in the line emitting gas (see e.g. Peterson et al., 2004; Sulentic et al., 2006; Vestergaard & Peterson, 2006), allowing what are thought to be the most reliable estimates of black hole mass in low  $z$  quasars. This approach has motivated us to seek similar measures in sources with the highest possible redshift rather than using other lines as  $H\beta$  surrogates.

In this paper we leave aside inter-line comparisons and focus on the  $H\beta$  spectral range in low and in intermediate-to-high  $z$  quasars ( $z \gtrsim 1$ ). Near IR spectra of the latter were obtained with the infrared spectrometer ISAAC on ESO VLT Unit 1. The high S/N and resolution of the new observations allow a meaningful comparison with measures obtained for low  $z$  sources. Low  $z$  measures come from two samples: (1) an atlas of bright sources with  $z \lesssim 0.8$  (Marziani et al., 2003a, hereafter, ATLAS sample) and (2) a magnitude-limited sample of 321 SDSS quasars ( $m_g < 17.0$ ,  $z < 0.7$  from Zamfir et al., 2008, hereafter SDSS sample).

In two previous papers we focused on a search for luminosity effects involving  $H\beta$ , FeII<sub>opt</sub>, and [OIII] $\lambda$ 4959,5007 (Sulentic et al., 2004, hereafter Paper I) as well as on the use of  $H\beta$  as a virial black hole mass estimator (Sulentic et al., 2006, hereafter Paper II). This paper presents observations and reductions for 30 additional sources ( $z = 1.08 - 3.09$ ; §2). We briefly discuss the  $H\beta$ , FeII and narrow line measures (§3) and then show that the addition of 27 new sources to the VLT sample reinforces the luminosity trends described in Paper I (§4). We then consider the distribution of VLT sources in the optical plane of 4DE1. Median 4DE1 and luminosity binned composite spectra are discussed in the context of the 4DE1 Population A-B concept

(Sulentic et al., 2000a, 2008). In §5 we use the binned composite spectra to decompose  $H\beta$  and make estimates of black hole mass  $M_{BH}$  and Eddington ratio  $L_{bol}/L_{Edd}$  for Pop. A and B sources.

## 2. Observations and Data Reduction

Spectra for intermediate-high redshift sources were obtained between 07/2004 and 07/2006 in service mode with the infrared spectrometer ISAAC mounted on VLT1 (ANTU) at the European Southern Observatory. Table 1 summarizes the new observations. The basic format is given below the Table, following almost exactly Tab. 1 of Paper II. In addition to the format provided below Table 1 we note that Col. (3) lists the blue apparent magnitude taken from Hamburg-ESO survey papers (Reimers et al., 1996; Wisotzki et al., 2000) while Col. (4) lists the source redshift  $z$  computed as described in section 2.2. Col. (8) lists the radio-loudness parameter  $R_K$  defined as the ratio between the specific flux at 6 cm and 4400 Å in the rest frame. We applied a  $k$ -correction for both the radio and optical data. In the case of the radio data:  $f_{e,6cm} = f_{v,obs} \cdot [\nu_{obs}(1+z)/\nu_{6cm}]^\alpha$  where the radio spectral-index is  $\alpha = 0.5$ . Only 14 of the sources have radio detections; 1.4GHz upper limits were derived for undetected sources from the NVSS detection threshold or the Sydney University Molonglo Sky Survey (SUMSS; Bock et al., 1999). Two sources are formally radio-loud following our definitions (Zamfir et al., 2008).

Each spectrum corresponds to a wavelength range (IR windows sZ, J, sH, sK; Col. (10) of Tab. 1) that covers all or part the region involving  $H\beta$  FeII $\lambda$ 4570 and/or FeII $\lambda$ 5130. Reduction of quasar spectra and standard stars followed exactly the same procedures described in Papers I and II. Wavelength calibration yielded rms residuals of 0.4, 0.6 and 0.9 Å in the sZ, J and sH windows, respectively. Absolute flux measures will be inaccurate because atmospheric seeing almost always exceeded the slit width ( $\approx 0''.6$ ) resulting in significant light loss. Small offsets were present in the wavelength calibration because the arc lamp frames were obtained in daytime and therefore usually after grism movement. A correction for these shifts was obtained by measuring the centroids of 2–3 OH sky lines against the arc calibration and calculating the average difference.

### 2.1. Sample Considerations

All 53 sources in the VLT-ISAAC sample were selected from the Hamburg-ESO (HE) quasar survey which was a color-selected and magnitude-limited ( $m_B \approx 17.5$ ) quasar survey (Wisotzki et al., 2000). Thirty-one new spectra are presented for 30 sources in §1 with 27 sources not previously observed. They are merged with Paper I and II measures to yield a total sample of 53 sources. Two of the new observations involve previously observed sources that were discussed in Paper I. The independent pairs of measures provide a valuable consistency check and are treated as independent data points in our statistical analysis of §4. Two new spectra obtained for HE 1505+0202 are listed in Table 1 with average values used in the analysis. HE 0353-3919 (Paper I) has been excluded from quantitative analysis because its  $H\beta$  profile is compromised by a gap in coverage between the sZ and Z bands (see Fig. 2 of Paper I). The resultant sample of 52 sources (and 54 data points) is henceforth referred to as the ISAAC sample.

The samples of Marziani et al. (2003a, ATLAS) and Zamfir et al. (2008, SDSS) are used as low- $z$  spectroscopic comparison samples. SDSS is more complete, involving the 321

brightest  $g$ -band selected ( $\leq 17.0$ ) in SDSS DR5 with  $z \leq 0.7$  while the ATLAS sample involves a more heterogeneous selection of 215 quasars largely brighter than  $m_B = 16.5$ . We make wide use of the SDSS sample in this study because of its higher level of completeness, larger number of sources, and because results from the ATLAS sample were already presented in Paper I and II. Both the SDSS and ATLAS data enable: (1) accurate measurements of  $H\beta$  and  $\text{FeII}_{\text{opt}}$  emission, (2) decomposition of the broad  $H\beta$  profile, and (3) measures of the narrow  $H\beta$  component ( $H\beta_{\text{NC}}$ ) and  $[\text{OIII}]\lambda\lambda 4959, 5007$  lines. The SDSS sample suffers a strong Malmquist bias. The ATLAS sample shows a more uniform luminosity distribution making a correlation analysis less biased. It will be used in the analysis of luminosity trends involving FWHM  $H\beta$  (§5).

## 2.2. Data Analysis

Analysis of ISAAC spectra made use of IRAF tasks to accomplish continuum and  $\text{FeII}_{\text{opt}}$  modeling as well as subtraction. The `specfit` task was employed to make a reliable model of the  $H\beta$  spectral region. The simultaneous fitting of continuum and FeII should be less dependent on subjective evaluations by the observer. We assume that the continuum underlying the  $H\beta$  spectral region is a power law of variable slope. Continuum subtraction has severe limitations due to the small bandwidth of our spectra and to (unknown) internal reddening effects. However, `specfit` usually found a plausible continuum (see Fig. 1). Estimation of continuum subtraction uncertainty due to S/N involves choosing continuum fluxes at about  $-3\sigma$  (minimum) and  $+3\sigma$  (maximum) levels where  $\sigma$  is the standard deviation of the most likely continuum choice. Uncertainties of continuum placement were empirically defined from the difference between extreme high/low continua and the most probable one derived by `specfit`.

$\text{FeII}_{\text{opt}}$  emission was modeled using a scaled and broadened template as previously employed by Marziani et al. (2003a). An important change was introduced to the FeII template emission underlying  $H\beta$  as described below (§2.3). We stress again that a notable advantage of `specfit` is that the scaled and broadened template can be simultaneously fit over  $\approx 1000 \text{ \AA}$  with a power-law continuum, the  $H\beta$  profile and the narrow lines ( $H\beta_{\text{NC}}$ ,  $[\text{OIII}]\lambda\lambda 4959, 5007$ ,  $\text{FeVII}\lambda 5160$ ,  $\text{FeVII}\lambda 5177$ ). The strong FeII blue blend (4450–4680  $\text{ \AA}$ :  $\text{FeII}\lambda 4570$ ) was measured as an estimator of the  $\text{FeII}_{\text{opt}}$  strength. The Gaussian broadening factor from the best fitting template yields an estimate of FWHM FeII. A careful estimate of minimum and maximum plausible broadening factors was made to derive  $\pm 3\sigma$  uncertainties. The blue side of the spectrum including  $\text{FeII}\lambda 4570$  is missing or only marginally covered in several sources. In these cases the best template fit was achieved for the red blend ( $\text{FeII}\lambda 5130$  in the range 5200–5600  $\text{ \AA}$ ) and  $\text{FeII}\lambda 4570$  was estimated assuming a fixed ratio between the red and blue blends. Fig. 2 shows the estimated FeII emission (green lines).

The  $H\beta$  profile was modelled with: (1a) a core Lorentzian component plus a weaker/broader Gaussian on the blue (usually) or on the red side of the core or, alternatively, (1b) the sum of two Gaussians one always very broad and showing non-negligible velocity shift relative to a narrower core component; (2) a narrow component ( $H\beta_{\text{NC}}$ ). We do not attribute any physical meaning to the “blind” decompositions performed with `specfit` in the case of the double Gaussian fits for individual sources. The two types of fit provide the simplest *empirical* description of broad  $H\beta$  profiles in the majority of sources. The  $H\beta$  profile was fit with a high order spline function (IRAF task `sfit`) in a few cases where the

model fits showed significant deviations from the actual profile. Spline functions do not yield a model fit but only an empirical fit that smooths noise and reproduces the main features and inflections in  $H\beta$ . The spline fit approach was the one used in our previous work (Marziani et al., 2003a) where sources with  $\text{FWHM } H\beta \leq$  and  $\geq 4000 \text{ km s}^{-1}$  favored Lorentzian and double Gaussian fits respectively. Systematic differences in flux and  $W$  measurements as well as in line profile parameters between the empirical and `specfit` approach occur since the extended wings of Gaussian and especially Lorentzian profiles lead to a lower continuum placement. The effect however is within the estimated measurement uncertainty.

The  $[\text{OIII}]\lambda\lambda 4959, 5007$  lines were also simultaneously modelled with the following conditions strictly enforced during the fitting procedure: (1) the flux ratio between  $[\text{OIII}]\lambda 5007$  and  $[\text{OIII}]\lambda 4959 \approx 3$ , (2) both lines should show identical profiles. It was often necessary to include a “semi-broad” and/or blueshifted component to model the  $[\text{OIII}]\lambda\lambda 4959, 5007$  profile since evidence for a strong blue asymmetry was observed in several cases. This approach yields a satisfactory reproduction of the observed  $[\text{OIII}]\lambda\lambda 4959, 5007$  profiles within our resolution and S/N limits. It is again an empirical method to properly estimate the total  $[\text{OIII}]\lambda\lambda 4959, 5007$  strength and describe the line profile shape. We do not make any assumptions about the actual nature of  $[\text{OIII}]\lambda\lambda 4959, 5007$  emission which will be the subject of a separate paper.

## 2.3. The $\text{FeII}_{\text{opt}}$ template

Considerable attention has been given to theoretical and empirical estimation of  $\text{FeII}_{\text{opt}}$  emission in the spectral region of  $H\beta$ , for a number of scientific (i.e., obtain a diagnostic of the BLR) and technical goals. Theoretical calculations of FeII emission, assuming the predominance of photoionization in the Broad Line Region have greatly improved in the last decade (Sigut & Pradhan, 2003; Sigut et al., 2004; Verner et al., 1999) with a 371-level model of the  $\text{Fe}^+$  ion presently included in the photoionization code CLOUDY v. 07.01 (Ferland et al., 1998). A detailed analysis of the FeII emission in I Zw 1 (Véron-Cetty et al., 2004) revealed rich and complex emission from several line systems, each associated with a well-defined redshift and FWHM. In the case of sources with larger FWHM and data with intermediate resolution as well as average S/N an analysis as detailed as that made for I Zw 1 (Véron-Cetty et al., 2004) cannot be done. The  $\text{FeII}_{\text{opt}}$  template approach works satisfactorily for the heterogeneous variety of type-1 AGN (Boroson & Green, 1992; Marziani et al., 2003a; Zamfir et al., 2008) with the probable exception of some outliers and extremely strong FeII emitters.

There is however a major problem associated with the empirical template: it is difficult to estimate the FeII emission under the  $H\beta$  line. Our empirical template differs from that of Boroson & Green (1992) because of lower FeII emission under  $H\beta$  and from Véron-Cetty et al. (2004) for the opposite reason. The new analysis of the I Zw 1 spectrum by Véron-Cetty et al. (2004), coupled with photoionization models, suggests that emission under  $H\beta$  should not be very strong. Therefore, the strength of the FeII lines underlying  $H\beta$  has been computed with an appropriate photoionization model. In the context of photoionization the present understanding of the FeII emitting region suggests low ionization and high electron density (Verner et al., 1999; Bruhweiler & Verner, 2008). We assumed an ionization parameter  $\log \Gamma = -2.25$ , and electron density  $[\text{cm}^{-3}] \log n_e = 12.75$ . This model provides an intensity ra-

tio between  $\text{FeII m29}$  and  $H\beta$  consistent with that measured in I Zw1. These improvements in the template do not significantly affect our  $R_{\text{FeII}} = F(\text{FeII}\lambda 4570)/F(H\beta) \approx W(\text{FeII}\lambda 4570)/W(H\beta)$  measurements. Even in the strongest  $\text{FeII}$  emitters ( $R_{\text{FeII}} \gtrsim 1$ ) the change in  $H\beta$  intensity is much lower than the associated uncertainty. The effect on  $H\beta$  profile is to lower the  $\text{FeII}_{\text{opt}}$  subtraction on the red side of  $H\beta$  making it stronger. The change with respect to the previous template is negligible in the case of weak emission but may not be so if  $\text{FeII}$  is strong and relatively narrow (see §4.2). A blueshifted, broad component ascribed to a wind (Sulentic et al., 2002; Marziani et al., 2008) is affected qualitatively by the new  $\text{FeII}_{\text{opt}}$  subtraction, although there are several examples of individual ISAAC sources (HE0248–3628, HE0512–3329 in Paper II) that unambiguously confirm the existence of such a component which is obvious in  $\text{Ly}\alpha$  and especially  $\text{CIV}\lambda 1549$  for several low- $z$  sources (Marziani et al., 2008).

### 3. Reduced Spectra and Line Measures

#### 3.1. Redshift Determination and Rest Frame Corrections

Rest frame determination is important in quasar spectroscopy because both broad and narrow emission lines are known to show velocity displacements relative to one another. We followed our standard procedure (Marziani et al., 2003a) and adopted the  $H\beta$  peak redshift ( $\lambda = 4861.33 \text{ \AA}$ ) as rest frame for our new sources. The  $[\text{OIII}]\lambda\lambda 4959, 5007$  lines ( $\lambda \approx 4958.9, 5006.85 \text{ \AA}$ ) were only used when they gave the same value as  $H\beta$  (see Col. (6) of Tab. 1). They sometimes show a blueshift relative to the  $H\beta$  peak and are designated as “blue outliers” in extreme cases (Zamanov et al., 2002; Marziani et al., 2003b; Aoki et al., 2005; Boroson, 2005; Komossa et al., 2008). Blue outliers usually show  $\text{FWHM } H\beta < 2000 \text{ km s}^{-1}$  but caution should be used when adopting  $[\text{OIII}]\lambda 5007$  or  $H\beta$  for rest frame determination (see also Hu et al., 2008a, who suggest a systematic  $\text{FeII}_{\text{opt}}$  redshift with respect to the quasar rest frame). The adopted  $z$  estimates were used to de-redshift the spectra while the IRAF dopcor task applied a  $(1+z)^3$  correction to convert observed specific fluxes into rest frame values. Fig. 1 shows the flux and wavelength calibrated spectra.

#### 3.2. Optical $\text{FeII}$ Lines

Fig. 2 shows the continuum subtracted spectra (left panels) with the adopted  $\text{FeII}_{\text{opt}}$  template model superimposed. Tab. 2 provides flux and equivalent width of  $H\beta$ , as well as flux and FWHM of  $\text{FeII}\lambda 4570$ . The data format is explained in the footnotes of each table. Care should be applied in using the FWHM values for  $\text{FeII}\lambda 4570$ . These values were obtained through a  $\chi^2$  minimization in the `specfit` procedure and therefore should at least be free of any subjective bias. Uncertainties were estimated by superimposing a sequence of templates with different FWHM values on the optimal  $\text{FeII}\lambda 4570$  spectrum and estimating the  $\pm 3\sigma$  confidence levels where FWHM  $\text{FeII}$  became unacceptably large or small. We find that  $\text{FWHM}(\text{FeII}\lambda 4570)$  is systematically smaller than  $\text{FWHM}(H\beta)$  and that the median value is  $\approx 4000 \text{ km s}^{-1}$ . Uncertainties of individual  $\text{FeII}$  measurements are quite large allowing only statistical inferences to be made.

#### 3.3. Narrow Lines

Table 3 reports the flux and equivalent widths values for  $H\beta_{\text{NC}}$  and  $[\text{OIII}]\lambda 5007$ .  $H\beta_{\text{NC}}$  is weak/marginal in most sources and

undetected in 4 sources. The total flux values for  $[\text{OIII}]\lambda 5007$  often include narrow and semi-broad components which are required to adequately fit the  $[\text{OIII}]\lambda\lambda 4959, 5007$  line profiles using `specfit`. Differences between the  $H\beta_{\text{NC}}$  and  $[\text{OIII}]\lambda\lambda 4959, 5007$  profiles indicate that crude intensity ratios  $[\text{OIII}]\lambda 5007/H\beta_{\text{NC}}$  may not be meaningful. The ratio  $[\text{OIII}]\lambda 5007/H\beta_{\text{NC}}$  has a clear meaning only if there is a redshift and FWHM consistency between  $[\text{OIII}]\lambda\lambda 4959, 5007$  and  $H\beta$ .

#### 3.4. $H\beta$ Line Profiles

Measurements of the broad  $H\beta$  profile including FWHM and other important line parameters such as asymmetry index, kurtosis and line centroid at various fractional intensities were obtained using a FORTRAN program developed for the purpose. These parameters are the same as defined in Paper I and are given in Tables 4 and 5. The right-hand panels of Fig. 2 emphasize the shape of  $H\beta$  for each source. Table 5 lists measurements of the  $H\beta_{\text{BC}}$  centroid at various fractional intensities (in  $\text{km s}^{-1}$ ). Each line measurement in Tables 4 and 5 is followed in the next column by its appropriate uncertainty at the  $2\sigma$  confidence level. The uncertainties on line profile parameters were estimated by changing the fractional height by  $\pm 0.05$ . All of these measures are affected by the compositeness of the broad  $H\beta$  profile which frequently shows unambiguous evidence for at least two distinct components: a broad component proper ( $H\beta_{\text{BC}}$ ) and very broad component ( $H\beta_{\text{VBC}}$  presumably from a very broad line region, VBLR). In the following, we will continue to refer to  $H\beta$  as the total broad emission excluding  $H\beta_{\text{NC}}$ , and to  $H\beta_{\text{BC}}$  as to the  $H\beta$  emission after  $H\beta_{\text{VBC}}$  (and of course also  $H\beta_{\text{NC}}$ ) removal.

## 4. Results

#### 4.1. Luminosity Effects

$H\beta$  – Fig. 3 shows the distribution of  $H\beta$  profile measures as a function of bolometric luminosity where  $L_{\text{bol}} \approx 10 \cdot \lambda L_{\lambda}$  ( $\lambda = 5100 \text{ \AA}$ ) for the SDSS data. Bolometric luminosity was computed from  $z$  and  $m_{\text{B}}$  for the ISAAC sample because of the spectra uncertain flux scale. Figure 3a (upper left panel) shows the distribution of  $\text{FWHM}(H\beta)$  measures as a function of  $\log L_{\text{bol}}$  where low  $z$  measures come from the SDSS sample (Zamfir et al., 2008) and ISAAC sources are indicated by larger filled circles. The only obvious, well defined FWHM trend found over  $\sim 5$  decades of source luminosity involves an increase in the minimum FWHM  $H\beta$  with luminosity as previously reported in Paper I. Fig. 3a shows a systematic increase with  $\log L_{\text{bol}}$  of mean/median FWHM  $H\beta$  from mean/median  $3200/2550 \text{ km s}^{-1}$  to  $5075/4900 \text{ km s}^{-1}$  which is likely driven by the minimum FWHM trend. No trend is observed, for example, among sources with  $\text{FWHM} > 4000 \text{ km s}^{-1}$ . The excess of sources with  $\text{FWHM} > 8000 \text{ km s}^{-1}$  in the range  $\log L_{\text{bol}} = 45.5 - 46.5$  simply reflects Malmquist bias amplified by the increase of sources above  $\log L_{\text{bol}} \approx 45.5$  due to the onset of strong source evolution in the range  $z = 0.5 - 0.7$ . The correlation of FWHM  $H\beta$  with source luminosity is weak (c.f. Paper I) but statistically significant for the increased samples of this paper, with Pearson’s correlation coefficient  $r \approx 0.26$  ( $P \lesssim 10^{-6}$ ).

Figure 3b (upper right) shows the distribution of asymmetry index (A.I.) as a function of luminosity. An excess of red asymmetric profiles is seen at all luminosities but does not show up well in the mean or median values which lie in the range  $0.03 - 0.06$  because of the strong SDSS source concentration between  $\text{A.I.} = \pm 0.05$ . The ISAAC sample shows the highest (reddest)

mean and median values with A.I. = 0.11 and 0.09, respectively. If we focus on the sources with more extreme A.I. values then we find the largest difference between the “strips”  $-0.4 < \text{A.I.} < -0.2$  and  $0.2 < \text{A.I.} < 0.4$ : red asymmetries outnumber blue ones by a factor of seven. Only 17 SDSS sources (zero ISAAC) show blue asymmetries greater than  $-0.2$  while  $\approx 85$  show red asymmetries greater than  $+0.2$  (17 ISAAC). No luminosity correlation is detected with the red asymmetric excess visible at all luminosities.

Figures 3c (lower left) and 3d (lower right) show the distributions of  $H\beta_{\text{BC}}$  “peak”  $c(\frac{3}{4})$  and “base”  $c(\frac{1}{4})$  profile velocity displacements (line shifts), respectively.  $c(\frac{1}{4})$  shows a strong source concentration around zero (unshifted profile base) but a significant excess of redshifts at all luminosities. There is evidence for a trend with mean/median values increasing from 56/57  $\text{km s}^{-1}$  in the lowest luminosity decade to 671/292  $\text{km s}^{-1}$  for the ISAAC sample. Thirteen sources (7 ISAAC) show base redshifts between 2000–4000  $\text{km s}^{-1}$  while no sources show blueshifts in that range. Clearly the red excess in Figures 3b and 3d are related. If we distinguish between radio quiet (RQ) and radio loud (RL) sources (Zamfir et al., *in preparation*) we find the striking absence of a RL source concentration near zero. Radio loud sources span the full range of observed red and blueshifts however with a preference for redshifts. The concentration around zero is a pure RQ effect.

The centroid  $c(\frac{3}{4})$  shows only a small number of sources with shifts above  $\pm 1000 \text{ km s}^{-1}$  (4 red and 7 blue and 0 ISAAC). The approximately 2 for 1 preference for blueshifts is confirmed in the range  $c(\frac{3}{4}) = 600 - 1000 \text{ km s}^{-1}$  with 8 red and 15 blueshifted sources. Mean values are slightly blue for lower luminosities ( $-20$  to  $-40 \text{ km s}^{-1}$  for  $\log L_{\text{bol}} \lesssim 46$ ) and become slightly red in the highest luminosity SDSS and ISAAC bins ( $+35 \text{ km s}^{-1}$ ). The simplest accretion disk models predict redshifted profile bases and blueshifted peaks (Chen et al., 1989; Eracleous & Halpern, 2003) leaving open the possibility that an underlying disk signature is present in all sources. Later discussion however does not support that conclusion for redshifted and red asymmetric profiles. The absence of strong luminosity correlations in Figure 3 is confirmed by Pearson and Spearman correlation coefficients.

[OIII] $\lambda\lambda 4959, 5007$ – Perhaps the most striking difference between the SDSS and ISAAC samples involves the relative weakness of narrow line emission in  $\approx 80\%$  of the latter. Table 3 shows only three ISAAC sources with  $W([\text{OIII}]\lambda 5007) \gtrsim 13 \text{ \AA}$ . We previously found (Sulentic et al., 2000b) mean values for low  $z$  sources in the range  $W([\text{OIII}]\lambda 5007) = 23 - 27 \text{ \AA}$  with standard deviations for various subsamples in the range  $10 - 30 \text{ \AA}$ . Only one source in the ISAAC sample shows  $W([\text{OIII}]\lambda 5007)$  greater than the mean of the low  $z$  sample: HE 0109-3518 with  $W([\text{OIII}]\lambda 5007) \approx 38.5 \text{ \AA}$ , an extremely large value especially considering the high luminosity of this  $z \approx 2.4$  quasar. This is the ISAAC source (Figure 1) that most closely resembles a low  $z$  quasar. Twelve blue outliers identified by Marziani et al. (2003b) show  $W([\text{OIII}]\lambda 5007) \approx 7.5 \text{ \AA}$  which is the same as the mean value for the sources listed in Table 3. There is a high fraction of sources in the ISAAC sample that may show a systematic blueshift with respect to  $H\beta_{\text{NC}}$ , making several ISAAC sources similar to the blue outliers in terms of the [OIII] $\lambda\lambda 4959, 5007$  properties. The issue will be however discussed in a separate paper.

#### 4.2. 4DE1 Parameters

A 4DE1 spectroscopic parameter space previously defined (Sulentic et al., 2000b, 2007) involves measures of  $\text{FWHM}(H\beta)$ ,  $R_{\text{FeII}}$  Civ. $\lambda 1549$  shift, and soft-X ray spectral slope (see also Boroson & Green, 1992). We focus here on the optical plane of 4DE1 where, as far as we can tell, none of the four principal parameters show a correlation with optical or UV luminosity out to  $z \approx 0.8$ . Fig. 4 shows the SDSS and ISAAC source distributions in the 4DE1 optical plane ( $\text{FWHM}(H\beta)$  vs.  $R_{\text{FeII}}$ ). Low- $z$  quasars are distributed along a curved sequence with sources showing both large  $\text{FWHM}(H\beta)$  and  $R_{\text{FeII}}$  apparently forbidden. The distribution of SDSS sources matches closely the one found in the ATLAS sample. The zone of occupation extends from the upper left where  $\text{FWHM}(H\beta)$  is large,  $\text{FeII}_{\text{opt}}$  is least prominent and  $\approx 50\%$  of the sources are RL. At the opposite (lower right) end we find sources with the narrowest  $\text{FWHM}(H\beta)$  profiles, strong  $\text{FeII}_{\text{opt}}$  and  $\sim 1\%$  radio loud sources. The centroid of the SDSS source distribution lies near  $\text{FWHM}(H\beta) = 3800 - 4000 \text{ km s}^{-1}$  and  $R_{\text{FeII}} = 0.3 - 0.4$ .

We use the 4DE1 optical plane to see if the higher luminosity ISAAC sample shows any difference in source distribution that might hint at a luminosity trend. ISAAC sources are shown as large dots with error bars in Fig. 4. The largest distribution differences involve: (a) the absence of ISAAC sources below  $\text{FWHM} \approx 3000 \text{ km s}^{-1}$  and (b) an apparent displacement of almost half of the ISAAC sample towards larger values of  $\text{FWHM}(H\beta_{\text{BC}})$  and  $R_{\text{FeII}}$ : on average by  $\approx 1 - 2000 \text{ km s}^{-1}$  in  $\text{FWHM}(H\beta_{\text{BC}})$  and by  $0.1 - 0.2$  in  $R_{\text{FeII}}$ . Difference (a) involves the previously discussed increase in minimum  $\text{FWHM}(H\beta_{\text{BC}})$  with luminosity and can be described as a zone of avoidance for high luminosity sources in the 4DE1 optical plane. Difference (b) requires more detailed study in the next section.

#### 4.3. 4DE1 Spectral Types and Composite Profiles

Further analysis of 4DE1 and source luminosity trends are best accomplished using composite spectra. This avoids confusion introduced by details in individual spectra and optimizes S/N. Composite spectra in the context of the optical 4DE1 plane have special value because  $\text{FeII}_{\text{opt}}$  prominence is one of the key parameters and  $\text{FWHM}(H\beta)$  is arguably the most reliable virial estimator of black hole mass. Fig. 4 is subdivided into bins of  $\Delta \text{FWHM}(H\beta) \approx 4000 \text{ km s}^{-1}$  and  $\Delta R_{\text{FeII}} \approx 0.5$ , following Sulentic et al. (2002).

Spectral types (bins) B1<sup>+</sup>, B4 and A3 each contain a single ISAAC source. A reexamination of the single B4 source HE1505+0212 suggests that  $\text{FeII}\lambda 4570$  emission is unusually strong with no reasonable continuum adjustment capable of moving it further to the left than bin B3. This source is either a genuine outlier or an extreme Pop. A source (following the luminosity-dependent boundary between Pop. A and B discussed in §4.5.1). Many ISAAC sources are located in bin B2 while SDSS sources are apparently rarer there and much more concentrated toward the lower left corner of the bin.  $R_{\text{FeII}}$  is relatively insensitive to small changes in the adopted continuum leading us to conclude that the displacement of ISAAC sources towards higher  $R_{\text{FeII}}$  cannot only be attributed to an effect of the data reduction. This supports the reality of distribution difference (b) discussed above.

#### 4.3.1. Decomposition and Fitting of ISAAC Spectra in the Optical Plane of 4DE1

Median composite ISAAC spectra were computed for sources in 4DE1 bins A1, A2, B1, B2 (Fig. 5) using calibrated and de-redshifted spectra normalized to specific flux of unity at 5100 Å. The first two composites show broader FWHM( $H\beta$ ) and the second two show stronger  $R_{\text{FeII}}$  compared to ATLAS (Sulentic et al., 2002) or SDSS composites for the same bins.

Pop. A sources can usually be modelled with a single unshifted Lorentzian component. This is also true for bin A1 and A2 ISAAC sources. Pop. B sources usually require a double Gaussian (unshifted broad  $H\beta_{\text{BC}}$  and redshifted very broad  $H\beta_{\text{VBC}}$  components: Sulentic et al., 2002).  $H\beta$  profiles in bin B1 and B2 sources are best fit with a double Gaussian model implying that both unshifted  $H\beta_{\text{BC}}$  and redshifted  $H\beta_{\text{VBC}}$  components seen in low  $z$  quasars are also present in high luminosity sources (Fig. 6). The decomposition is not always unique and it can therefore be difficult to estimate the relative contributions of the two components. An important clue about the proper decomposition comes from profile variations in the source PG1416–129 (Sulentic et al., 2000c, see also 3C 206 in Corbin & Smith (2000)) where the  $H\beta_{\text{BC}}$  almost disappeared following a continuum decline while the  $H\beta_{\text{VBC}}$  showed less variation and was revealed much more clearly as very broad and redshifted. The highest S/N inflected spectra in the ISAAC sample (e.g. HE0109–3518) also clearly favor this decomposition which is adopted throughout our analysis.

#### 4.4. Luminosity Binned Spectra

Comparing mean or median spectra for random samples of quasars observed in different luminosity ranges is unlikely to yield meaningful results. Any difference would be obscured by the intrinsic dispersion of spectral properties at any given apparent luminosity. As stressed in much of our previous work (see especially the review by Sulentic et al., 2000a), and illustrated again in Fig. 5, all quasar spectra are not self-similar. Figure 3a reinforces this point in one dimension by showing that FWHM  $H\beta$  spans a very large range from  $\approx 500 \text{ km s}^{-1}$  to  $\approx 20000 \text{ km s}^{-1}$ . We suggest that a *minimum requirement* for physically meaningful comparisons among low- $z$  samples involves distinguishing between 4DE1 Pop. A and B sources. More refined comparisons becomes possible by generating composite spectra for individual Pop. A and B bins: e.g. A1, A2, A3, ... and B1, B2, B1<sup>+</sup>, etc. The population A – B concept was perhaps the most controversial part of our 4DE1 formalism where sources were arbitrarily divided into population A and B based on FWHM  $H\beta$  profile measures above and below  $\approx 4000 \text{ km s}^{-1}$  respectively. However we find a multitude of differences when we distinguish sources this way (Sulentic et al., 2007). Most RL sources belong to Pop. B, and about 25–30% of RQ sources also belong to Pop. B, but the Pop. A/B distinction appears to be more effective than more traditional RQ vs. RL comparisons in terms of BLR structure.

Fig. 7 shows median composite spectra in six luminosity intervals using 321 SDSS and 53 ISAAC sources. Composites were generated separately for Pop. A and B sources in decades of  $\log L_{\text{bol}} = 43 - 44$  to  $48 - 49$ . All ISAAC sources lie in the interval  $\log L_{\text{bol}} = 47 - 49$  with a small number creating the highest  $L_{\text{bol}}$  bin ( $48 - 49$ ). Pop A and B quasars show parallel trends with increasing luminosity:  $[\text{OIII}]\lambda\lambda 4959, 5007$  and  $H\beta_{\text{BC}}$  systematically decrease in equivalent width but  $H\beta$  at the same time increasingly becomes redward asymmetric. The strong de-

crease in narrow line strength is expected from standard nebular theory (see e.g. Netzer, 1990, with the caveats of Sulentic et al. (2007)). The Eigenvector 2 anti-correlation between strength of  $\text{HeII}\lambda 4686$  and luminosity (Boroson & Green, 1992) is also seen. No obvious trend involving  $\text{FeII}_{\text{opt}}$  is seen which reflects the orthogonality of luminosity with respect to Eigenvector 1 measures using principal component analysis (PCA). The ISAAC sample median spectra are most similar to the highest luminosity SDSS bin composite. The change in  $H\beta$  towards high luminosity appears to be concentrated in the strength of the red side of the line which was already anticipated as a red asymmetry and line base  $c(\frac{1}{4})$  red shift in Figures 3b and 3c.

#### 4.4.1. Decomposition of Luminosity Binned Spectra

The next logical step is to decompose and quantify individual lines and line components in different Pop. A and B luminosity bins. Earlier attempts revealed one of the most obvious differences among low redshift  $H\beta$  profiles and provided one of the motivations for the population A–B concept (Sulentic et al., 2002; Marziani et al., 2003b; Sulentic et al., 2007). Fig. 8 shows Pop A and B median spectra binned in luminosity after continuum subtraction. Tab. 6 provides line equivalent width measures and FWHM  $\text{FeI}$  values for various spectral bins discussed in the text. Tab. 7 tabulates line profile measures and Tab. 8 provides  $H\beta$  centroid measures and estimated uncertainties for the same bins. Formats appear as footnotes below each table. The first seven lines present various 4DE1 bin values for ISAAC sources while the remainder provide luminosity bin values following the designations in Fig. 4. Measures in these tables reflect the results of simultaneous fits to all lines and components in each median composite spectrum. Attempts at a sequential line-by-line decomposition yielded very similar results. Numbers quoted in the discussion of Figure 3 are averages or medians based on individual source measures while Tables 6, 7, 8 give values derived from composite spectra. There are no significant discrepancies between measures estimated in these two ways. Source codes for  $L_{\text{bol}}$  bins use the first two digits of the  $L_{\text{bol}}$  bin followed by A or B for the population (e.g. values for line 43A correspond to measures of the Pop. A luminosity composite for  $\log L_{\text{bol}} = 43 - 44$ ). Narrow line changes with luminosity will be discussed in a separate paper so that we can concentrate on the properties of  $H\beta_{\text{BC}}$  and  $H\beta_{\text{VBC}}$ . FWHM  $H\beta$  in Pop. A sources shows a systematic increase with  $L_{\text{bol}}$  from  $2000 \text{ km s}^{-1}$  to  $4100 \text{ km s}^{-1}$  across the six luminosity bins likely driven by the increase in minimum FWHM  $H\beta$  with  $\log L_{\text{bol}}$  shown in Figure 3a.

Pop. B shows no clear FWHM trend with  $\log L_{\text{bol}}$  but we find that  $W(H\beta)$  decreases systematically with increasing luminosity. Pop. A does not show an obvious trend although  $W(H\beta)$  is smallest in the most luminous Pop. A bins. The Pop. B “Baldwin Effect” shows  $W(H\beta)$  decreasing from  $143 \text{ \AA}$  to  $82 \text{ \AA}$  with increasing  $\log L_{\text{bol}}$ . Pop. B sources show 6–7 times larger asymmetry indices at the highest source luminosities as well as evidence for a redshift near the base ( $c(\frac{1}{4})$ ) of the line. The mean velocity redshift increases by 9 times from the lowest to highest luminosity bin. Fig. 9 shows the increase with source luminosity of the fraction of  $c(\frac{1}{4})$  redshifts for Pop. B sources. The excess flux in the red wing of  $H\beta$  is revealed in Fig. 8 decompositions to be a real  $H\beta$  flux excess and not due to  $\text{FeII}_{\text{opt}}$  contamination (see also Netzer & Trakhtenbrot, 2007, who found a similar result).

Conversely  $\text{FeII}_{\text{opt}}$  subtraction reveals that  $H\beta$  shows little evidence for profile shifts and asymmetries in Pop. A sources. The apparent Pop. A red asymmetry appears to increase with

luminosity in Figure 7; however Figure 8 suggests that it is mainly due to  $\text{FeII}_{\text{opt}}$  and  $[\text{OIII}]\lambda\lambda 4959, 5007$  contamination on the red side of  $H\beta$ . Table 6 shows that  $W(\text{FeII}\lambda 4570)$  does not increase with luminosity but  $H\beta_{\text{BC}}$  decreases somewhat making red  $\text{FeII}_{\text{opt}}$  contamination appear to grow in strength, even if some redward, very broad emission cannot be excluded at a low flux level in the highest luminosity bins.

The quantification in Tables 6, 7, 8, and the two components required to model Pop. B sources, reinforce past evidence (Corbin, 1995; Sulentic et al., 2000c, 2002) for the existence of a redshifted very broad line component in  $H\beta$ . The  $H\beta_{\text{VBC}}$  is the most obvious profile difference between Pop. A and B, as well as between high and low luminosity sources in Pop. B. As noted earlier both RL and RQ sources are found in Pop. B and both Pop. B RL and Pop. B RQ sources show the  $H\beta_{\text{VBC}}$ . This provides a strong spectroscopic argument in favor of the importance of the Pop. A-B concept compared to comparisons on the basis of radio loudness. The effect of the VBLR component is to produce a broader, more red asymmetric and redshifted  $H\beta$  profile with the amplitude of these effects dependent on the relative strengths of the BLR and VBLR components. HE 0109–3518 in Fig. 1 is an example of a source with a weak/moderate VBLR component while HE 1039–0724 shows one of the strongest VBLR components in the ISAAC sample. Tab. 7, 8, Fig. 9, and the profile decompositions in Figure 8 show evidence for a uniform increase of  $H\beta_{\text{VBC}}$  strength with luminosity.

#### 4.5. Luminosity Dependence of Spectral Types

The left-hand panel of Fig. 10 shows the bolometric luminosity distributions for ISAAC sources showing  $H\beta$  profile best fit with single Lorentzian and double Gaussian models. Ambiguous sources are excluded. A K-S test confirms that the two source luminosity distributions are not significantly different. The right panel shows the distribution of profile fits in an FWHM  $H\beta$  vs. bolometric luminosity plane with Lorentzian, double-Gaussian and ambiguous sources denoted L, G and U respectively. No strong luminosity preference is seen for L or G sources. The difference between FWHM distributions for L and G profiles is highly significant with a K-S test suggesting that  $P \lesssim 10^{-8}$  for sources with different profile shapes to be drawn from the same parent population. This can be taken as an independent confirmation of the Pop. A-B dichotomy.

##### 4.5.1. Spectral Types: A Refinement

The Pop. A-B  $\text{FWHM}(H\beta_{\text{BC}}) = 4000 \text{ km s}^{-1}$  boundary was adopted using a low  $z$  and low luminosity sample. There is no strong evidence that it has a direct physical meaning even if it is better motivated empirically than the limit at  $\text{FWHM}(H\beta) = 2000 \text{ km s}^{-1}$  used to separate “Narrow Line” Seyfert 1s (NLSy1s) from the rest of broad line AGN.

Fig. 11 presents a reprise of Figure 3a with a much expanded low redshift sample including: (a) SDSS DR5 quasars brighter than  $g=17.0$  within  $z=0.7$ , (b) FIRST radio detected SDSS DR5 quasars between  $g=17.0-17.5$  within  $z=0.7$  (Zamfir et al., 2008) and (c) the ATLAS sample of low redshift quasars (Marziani et al., 2003a). This provides a somewhat better mapping of the low  $z$  source distribution in the  $\text{FWHM} - \log L_{\text{bol}}$  plane. The SDSS quasar sample does not include sources with  $\text{FWHM } H\beta < 1000 \text{ km s}^{-1}$  which were classified in SDSS as galaxies. The narrowest of these “broad line” sources can be confirmed as Type 1 AGN (NLSy1) by the presence of  $\text{FeII}\lambda 4570$

emission in their spectra. Among the 400+ highest S/N SDSS quasars that we have studied in detail (Zamfir et al., 2008) all but five show detectable  $\text{FeII}_{\text{opt}}$  emission suggesting that the presence of optical  $\text{FeII}_{\text{opt}}$  emission is an ubiquitous property of Type 1 AGN. A recent survey (Zhou et al., 2006) of NLSy1s using SDSS DR3 provides a representative census of these sources. They found 41 sources ( $z \lesssim 0.7$ ) brighter than  $g = 17.5$  between  $\text{FWHM } H\beta = 450 - 2000 \text{ km s}^{-1}$  and these are indicated in Figure 11 with filled triangles. The old Pop. A-B and NLSy1-rest of Type-1 AGN “boundaries” at 4000 and 2000  $\text{km s}^{-1}$ , respectively are indicated. This figure provides us with a better defined lower edge to the  $\text{FWHM } H\beta$  distribution. We superpose curves corresponding to exponents  $a=0.52$  (Bentz et al., 2006) and 0.67 (Paper II) in the Kaspi relation which will be considered in the discussion. Fig. 11 also shows a revised Pop. A-B boundary following the form of an  $a = 0.67$  Kaspi relation as done in Paper I.

Figures 10 and 11 suggest a modified 4DE1 Pop. A/B boundary is required for high luminosity quasars. We define modified 4DE1 spectral types MA1, MA2, MB1, MB2, etc. where the boundary between the MA and MB Populations is now luminosity-dependent and given by  $\text{FWHM}_{\text{AB}} \approx 3500 + 625 \cdot L_{\text{bol}}^{0.165}$  ( $a = 0.67$ ; analogous to Paper I). Composite line  $H\beta$  profiles for the revised 4DE1 bins are similar to those obtained with the fixed FWHM definition (Fig. 5 and Fig. 6) and are therefore not shown.

In order to decide whether the fixed ( $4000 \text{ km s}^{-1}$ ) or luminosity dependent boundary is more significant we defined three samples: (1) the old Pop. A, (2) an intermediate population between  $4000 \text{ km s}^{-1}$  and new luminosity-dependent limit and (3) a modified Pop. B  $\text{MB} \equiv B \setminus M$ . We can also consider a modified Pop. A,  $\text{MA} \equiv A \cup M$ . The  $H\beta$  spectral region before and after continuum subtraction for the median spectra of A, M and MB are shown in Fig. 12 and Fig. 13 respectively. The M median most closely resembles the Pop. A median rather than MB (or B). Fig. 12 and 13 show that the M  $H\beta$  spectral region resembles the one of Pop. A, and that the  $H\beta$  fit is well fit by a Lorentzian function, as it is the case for Pop. A sources. This suggests that the luminosity dependent limit  $\text{FWHM}_{\text{AB}}(L)$  might be more appropriate. The distribution of G and L sources in the  $\text{FWHM}(H\beta_{\text{BC}})$  vs. luminosity plane (Fig. 10) also supports this result. Although individual fits should be treated with caution we see that the shapes are predominantly Lorentzian in the Pop. A and M regions while they are Gaussian in the MB area of the plane.

#### 4.6. Black Hole Mass and Eddington Ratio

$\text{FWHM}(H\beta)$  has been used as a virial estimator of  $M_{\text{BH}}$  (Vestergaard & Peterson, 2006) at low redshift. The problem is what to use above redshift  $z \approx 0.9$ . The use of  $\text{CIV}\lambda 1549$  as an  $H\beta$  surrogate involves problems that seriously reduce the reliability of high  $z$   $M_{\text{BH}}$  estimates (Sulentic et al., 2007; Netzer et al., 2007). We have chosen instead to follow  $H\beta$  out to the highest possible redshifts via infrared spectroscopy. We use the updated relationships linking  $\text{FWHM}(H\beta_{\text{BC}})$ , specific luminosity at 5100 Å and BLR radial distance  $R_{\text{BLR}}$  from Vestergaard & Peterson (2006, their Eq. (5)). We do not enter into the caveats of black hole mass and Eddington ratio determinations (see e.g. Collin et al., 2006; Sulentic et al., 2006; Marconi et al., 2008; Shen et al., 2008) remarking only that  $M_{\text{BH}}$  values are uncertain by a factor 2–3 at  $1\sigma$  confidence level if derived from single-epoch observations. It is also possible to infer bolomet-

ric luminosity from the specific continuum flux assuming a constant bolometric correction. One can therefore also estimate the luminosity-to-mass ratio ( $L_{\text{bol}}/M_{\text{BH}}$ ). This approach is very crude (see e.g. Hopkins et al., 2007; Kelly et al., 2008) but a bolometric correction is still relatively stable across RQ and most RL sources with the obvious exception of core-dominated (beamed) sources.

The distribution of ISAAC quasars with L- and G-type fits as a function of  $M_{\text{BH}}$  and  $L_{\text{bol}}/L_{\text{Edd}}$  are shown in the left- and right-hand panels of Fig. 14 respectively. Fig. 15 shows all ISAAC sources (including U  $H\beta_{\text{BC}}$  profiles) in the  $L_{\text{bol}}/L_{\text{Edd}}$  vs.  $M_{\text{BH}}$  plane. We derive quite large masses in the range  $\log M_{\text{BH}}=8.5$ –10.0 with a range of  $\log L_{\text{bol}}/L_{\text{Edd}} = -1.0$  to 0.0. L (assumed Pop. A) and G (assumed Pop. B) profiles favor lower/higher  $\log M_{\text{BH}}$  and higher/lower  $\log L_{\text{bol}}/L_{\text{Edd}}$  values, respectively, as previously found for our ATLAS sample (Marziani et al., 2003b). The difference in the distribution is significant for both  $M_{\text{BH}}$  and  $L_{\text{bol}}/L_{\text{Edd}}$ , with a low probability that sources with L- and G-type profiles come from the same parent distribution of  $L_{\text{bol}}/L_{\text{Edd}}$  and  $M_{\text{BH}}$ : K-S tests indicate a probability  $\lesssim 10^{-3}$ . However, there is a range of  $L_{\text{bol}}/L_{\text{Edd}}(-0.5 \div -0.3)$  where L- and G- type sources are almost equally represented. The absence of a sharp  $L_{\text{bol}}/L_{\text{Edd}}$  boundary can be understood in terms of error effects as well as of systemic biases. Typical uncertainty in  $\log L_{\text{bol}}/L_{\text{Edd}}$  is  $\approx 0.1$ , if one assumes that the bolometric luminosity is uncertain by 50%, and that the FWHM( $H\beta$ ) has typical error of 10%. However, this estimate neglects the scatter in the size-luminosity relationship for the BLR. In addition, orientation effects – which are established among radio loud quasars (see e.g., Sulentic et al., 2003; Rokaki et al., 2003) – may well raise the  $L_{\text{bol}}/L_{\text{Edd}}$  of several sources of Pop. B. They are not considered in the  $L_{\text{bol}}/L_{\text{Edd}}$  and  $M_{\text{BH}}$  estimates presented here. Moreover, the magnitude limit of our ISAAC sample makes possible that we can detect *only* Pop. B sources with the largest  $L_{\text{bol}}/L_{\text{Edd}}$  values (cf. Fig. 7 of Paper II).

Fig. 16 shows the dependence of  $c(\frac{1}{4})$  and A.I. on  $M_{\text{BH}}$  and  $L_{\text{bol}}/L_{\text{Edd}}$ . Significant correlations between  $M_{\text{BH}}$  and both A.I. and  $c(\frac{1}{4})$  are found while no significant correlations are found involving  $L_{\text{bol}}/L_{\text{Edd}}$ . The A.I. vs  $M_{\text{BH}}$  correlation is marginally significant ( $P \approx 4 \cdot 10^{-3}$ ) if Pop. B sources are considered alone; in this case  $c(\frac{1}{4})$  and  $M_{\text{BH}}$  are not significantly correlated. This is perhaps not surprising considering the small number of sources, the typical errors, the  $M_{\text{BH}}$  “segregation” between Pop. A and B. Median spectra in bins of  $M_{\text{BH}}$  and  $L_{\text{bol}}/L_{\text{Edd}}$  point toward the origin of the correlation with  $M_{\text{BH}}$  (Fig. 17). The bin labeled as  $\log M_{\text{BH}} < 9.5$  actually covers masses in the range  $8.5 \lesssim \log M_{\text{BH}} < 9.5$ , and for  $\log L_{\text{bol}}/L_{\text{Edd}} \lesssim -0.5$  corresponds to the bin  $3.9 \lesssim \log L_{\text{bol}}/M_{\text{BH}} \lesssim 4.4$  in Figure 9 of Marziani et al. (2003b). The remaining three bins represent the extension to higher masses and  $L_{\text{bol}}/L_{\text{Edd}}$  that were not sampled at  $z \lesssim 0.7$ . We see a trend, as observed at low- $z$ , that for fixed  $L_{\text{bol}}/L_{\text{Edd}}$  the redward component is stronger for larger  $M_{\text{BH}}$ . This result is discussed in §5.4.

## 5. Discussion

### 5.1. Luminosity Trends

One of the motivations for the ISAAC survey was to search for trends, or even correlations, between emission line properties and source luminosity. Another motivation was to compare high and low luminosity source properties in the 4DE1 context. PCA of a bright quasar sample (Boroson & Green, 1992) found source luminosity to be orthogonal to all line measures except

$W(\text{HeII}\lambda 4686)$ . An  $[\text{OIII}]\lambda 5007$  measure was included among the original Eigenvector 1 parameters (Boroson & Green, 1992) showing a large scatter likely due to the strong  $L_{\text{bol}}$  dependence that we find with ISAAC. We did not adopt an  $[\text{OIII}]$  measure in our 4DE1 formalism because we preferred to avoid narrow line considerations as much as possible (Sulentic et al., 2000b). Subsequent 4DE1 studies at low  $z$  (e.g., Paper I and references found no luminosity dependence on broad line LIL measures. What was thought to be the most significant (inverse) correlation between luminosity and broad line HIL measures (especially  $\text{CIV}\lambda 1549$ ) (Baldwin et al., 1978) is now known to be present in quasar samples with small redshift/luminosity dispersion (Xu et al., 2008) and is likely related to intrinsic source properties such as Eddington ratio (Bachev et al., 2004).

Only one luminosity trend was found over the 5-6 luminosity decades covered in this study (without Pop. A/B discrimination). Profile parameter distributions (Figure 3) are essentially the same at all luminosities. The one exception involves an increase in minimum FWHM  $H\beta$  with  $\log L_{\text{bol}}$  visible in Figure 3a (see also Paper I). Low luminosity ( $\log L_{\text{bol}} = 43.0$ ) sources show FWHM  $H\beta_{\text{BC}}$  values as low as 500–750  $\text{km s}^{-1}$  while the minimum value at  $\log L_{\text{bol}} = 48$  appears to be FWHM  $H\beta \approx 3000 \text{ km s}^{-1}$ . The lower FWHM  $H\beta$  limit is expected if broad Balmer line emission arises in a virialized cloud distribution (or accretion disk) that obeys a Kaspi (see e.g. Kaspi et al., 2005) relation. We can think of the minimum FWHM- $\log L_{\text{bol}}$  trend as the boundary for sources radiating sub-Eddington. NLSy1s defined (at low  $z$ ) as sources with FWHM  $H\beta < 2000 \text{ km s}^{-1}$  are absent from the ISAAC sample.

It is unclear if a Kaspi relation ( $R_{\text{BLR}} \propto L^{-a}$ ) is valid above redshifts of a few tenths. There has been much discussion about the correct exponent in the Kaspi relation with values between  $a = 0.5 - 0.7$  favored (Kaspi et al., 2000, 2005; Bentz et al., 2006). Figure 11 provides an empirical representation of the minimum FWHM  $H\beta$  trend. Note that the expected trend has been quadratically combined with the instrumental resolution (assumed to be 200  $\text{km s}^{-1}$  at FWHM, appropriate for the SDSS). Superposed curves corresponding to  $a = 0.52$  (Bentz et al., 2006), and 0.67 (Kaspi et al., 2005, Paper II) show that discrimination between these values becomes possible above  $\log L_{\text{bol}} \approx 47$ . A first impression is that  $a = 0.52$  is disfavored by the ISAAC data unless a considerable number of these sources are super-Eddington radiators. Thus values in the range  $a = 0.6-0.7$  are favored. However a complicating factor involves the dependence of FWHM  $H\beta$  on source orientation which is especially important if one accepts the paradigm of a line emitting accretion disk. Some low redshift sources with small FWHM  $H\beta$  (extreme NLSy1 sources) show rapid high amplitude X-ray variability (e. g. Brinkmann et al., 2003) or blue shifted narrow lines (blue outliers) which have been argued to signal near face-on orientation. In a previous paper (Marziani et al., 2003b) we attempted inclination corrections for blue outliers assuming a  $\sin i$  dependence of FWHM. Using a tentative correction that increases black hole mass by  $\Delta M_{\text{BH}} \approx 0.4$  we were able to move many apparently super-Eddington NLSy1 radiators (sources with  $\log L_{\text{bol}} \sim 46$  that lie below the  $a = 0.5$  curve in Figure 11) below  $L_{\text{bol}}/L_{\text{Edd}} = 1$ . It seems unlikely that more than a very few ISAAC sources involve preferred orientation (5 are nominally super-Eddington) given the distribution of observed FWHM  $H\beta$  values even if optical luminosity is orientation dependent. It is also possible that orientation becomes increasingly less important in higher  $L_{\text{bol}}$  sources because of radiative instability in the accretion disk (Blaes, 2007). A value as large as  $a = 0.67$  would imply that all quasars radiate well below the Eddington limit. We conclude that there is no



strong evidence for a population of super-Eddington radiators in our low  $z$  and ISAAC samples.

### 5.2. 4DE1 Populations A and B

This study suggests that, in order to isolate luminosity effects and other fundamental trends in quasar samples, one should work in the context of the 4DE1 formalism and take advantage of the Population A-B concept. The empirical evidence continues to grow in favor of two distinct populations of quasars. We recently summarized the multitude of empirical differences between the two populations (Sulentic et al., 2007, 2008). If luminosity trends exist for only one of the populations then the lack of a trend in the other might obscure the effect in a mixed sample such as the one displayed in Figure 11. The Pop A – B boundary was empirically defined, after noting a discontinuity between the sources whose  $\text{FWHM}(H\beta)$  lies in the range 2000 – 4000  $\text{km s}^{-1}$  and those of Pop. B (also because almost all RL sources are pop. B). The similarity in emission line parameters between those sources and the NLSy1s then suggested a single population for the entire 0–4000  $\text{km s}^{-1}$  range. In analogy with the minimum  $\text{FWHM } H\beta$  trend which corresponds to a fixed Eddington ratio of 1 we can expect that the limit between Pop. A and B will also be luminosity dependent (Paper I).

We have previously suggested that the Pop. A-B  $\text{FWHM } H\beta_{\text{BC}}$  boundary might reflect a critical accretion rate/Eddington ratio ( $L_{\text{bol}}/L_{\text{Edd}} \sim 0.2 \pm 0.1$ ). We note that a number of recent studies have independently arrived at a similar “critical”  $\text{FWHM}$  or  $L_{\text{bol}}/L_{\text{Edd}}$  value (Marziani et al., 2003b; Collin et al., 2006; Bonning et al., 2007; Kelly et al., 2008; Hu et al., 2008b). Such a critical value might signal a significant change in disk structure/kinematics that is reflected in systematically larger  $\text{FWHM } H\beta$ , the demise of a  $\text{Civ } \lambda 1549$  wind as well as weaker soft X-ray and FeII emission. It is interesting to point out that the thin accretion disk approximation is expected to break down at  $L_{\text{bol}}/L_{\text{Edd}} \lesssim 0.3$  with the development of an inner thick structure (Hubeny et al., 2000). This kind of change might well affect the spectroscopic signature of the BLR.

It is probably naïve to expect a luminosity dependence as strong as the one predicted by a fixed  $L_{\text{bol}}/L_{\text{Edd}}$  (Fig. 11). The Pop. A/B boundary is found to be close to 4000  $\text{km s}^{-1}$ , following four lines of evidence: (1) the median spectrum for Pop. A in the luminosity bin  $43 \lesssim \log L_{\text{bol}} \lesssim 44$  shows that the  $H\beta$  is Lorentzian; (2) between constant  $\text{FWHM}(H\beta)=4000 \text{ km s}^{-1}$  and the  $L_{\text{bol}}/L_{\text{Edd}}=0.15$  line, and for  $45 \lesssim \log L_{\text{bol}} \lesssim 47$ , most ATLAS sources show typical Pop. A properties. A minority of core-dominated radio-loud sources are located there since they are expected to be observed almost pole-on, at minimum  $\text{FWHM}$ . If  $44 \lesssim \log L_{\text{bol}} \lesssim 45$  ATLAS sources are mainly located within  $\sim 500 \text{ km s}^{-1}$  of  $\text{FWHM} = 4000 \text{ km s}^{-1}$ , their  $H\beta$  profiles are similar to but not exactly the same as the ones of Pop. A. In the present paper we consider the luminosity dependence of the boundary to follow Paper I assuming a  $\approx 0.67$ . It is assumed constant corresponding to  $\text{FWHM} \sim 4000 \text{ km s}^{-1}$  below  $\log L \approx 47$ .

### 5.3. An $H\beta_{\text{BC}}$ “Baldwin Effect” is Present only in Population B

The Pop. A/B concept provides a useful alternate way to evaluate luminosity properties. When we discriminate by source population we immediately find possible luminosity trends between  $\text{FWHM}$  and  $W(H\beta)$  for Pop. A and Pop. B respectively. The former trend sees a mean  $\text{FWHM } H\beta$  increase with luminosity from

$\approx 2000 \text{ km s}^{-1}$  up to  $\approx 4000 \text{ km s}^{-1}$ . This is likely driven by the minimum  $\text{FWHM } H\beta$  trend already discussed as well as by Malmquist bias since all of the highest luminosity sources lie at higher redshifts and are preferentially selected in a flux limited sample. Assuming an underlying correlation between black hole mass and source luminosity we expect systematically larger black hole masses for the ISAAC sources as is observed.

Pop. B sources show a decrease in  $W(H\beta)$  by almost a factor of two over our source luminosity range. This  $H\beta$  Baldwin effect is difficult to interpret because  $H\beta$  is a composite feature ( $H\beta_{\text{BC}} + H\beta_{\text{VBC}}$ ). Tab.6 presents an attempt at quantitatively separating BLR and VBLR components for the six Pop. B luminosity binned composite spectra. The same can be done for Pop. A but the BLR component always dominates  $H\beta$  in all luminosity bins. The BLR component in Pop. B ranges from 60% of  $H\beta$  at low luminosity to 25% at  $\log L_{\text{bol}} = 47 - 48$ . Correction for the VBLR component yields a “super” Baldwin effect where  $W(H\beta_{\text{BC}})$  decreases by a factor of four over our luminosity range. At the same time we find considerable scatter but no obvious trend in the strength of FeII emission as measured in the FeII  $\lambda 4570$  blend. The highest luminosity Pop. B sources with smallest  $W(H\beta_{\text{BC}})$  show an apparently more prominent  $H\beta_{\text{VBC}}$  while its contribution in low luminosity sources seems modest because  $H\beta_{\text{BC}}$  dominates.

The simplest interpretation of these results involves changes in physical conditions of the BLR emitting region due to: (1) source luminosity and (2) the Pop. A-B dichotomy. As alluded to above the first may involve changes related to radiation pressure dominance in the accretion disk at higher source luminosity and the second changes related to a critical Eddington ratio. The tendency for  $\text{FWHM}(\text{FeII})$  to follow  $\text{FWHM } H\beta_{\text{BC}}$  in BLR-dominated Pop. A sources can be taken as evidence for an FeII –  $H\beta$  BLR commonality. The inferred lower density of the VBLR (e.g., Sulentic et al., 2000c) in (less BLR dominated) Pop. B sources disfavors an FeII/VBLR emission region commonality (Marziani et al., 2008).  $W(H\beta_{\text{VBC}})$  is found to be approximately constant in the six luminosity bins suggesting that it arises largely in optically thick gas photoionized by the central continuum. The largest challenge is to explain the four-fold decrease in  $H\beta_{\text{BC}}$  strength observed only Pop. B sources. The simplest interpretation involves a change in Pop. B physical conditions that suppresses  $H\beta_{\text{BC}}$ . Since  $H\beta_{\text{BC}}$  and FeII are thought to arise in the same region this might point toward collisional quenching of  $H\beta$  BLR emission as originally suggested by Gaskell (1988). Another, even simpler possibility involves different sized annuli for FeII and  $H\beta_{\text{BC}}$  emitting regions. If we correct  $W(H\beta)$  measures for  $H\beta_{\text{VBC}}$  and recalculate  $R_{\text{FeII}}$  parameters we find that many/most Pop. B sources will move towards higher  $R_{\text{FeII}}$  values  $\approx 1$  in the 4DE1 optical plane. The similar  $R_{\text{FeII}}$  ratios observed in Pop. A luminosity bins (using  $H\beta_{\text{BC}}$  only) suggest also a similarity in physical conditions. In other words, we would have a similar low-ionization BLR in both Pop. A and B sources plus a second VBLR only in Pop. B sources.

### 5.4. Black Hole Mass and Eddington Ratio

Tab. 6 presents  $\text{FWHM } H\beta_{\text{BC}}$  estimates for Pop. B luminosity bins. The  $H\beta_{\text{BC}}$  of Tab. 6 is related to the “reverberating” component almost equivalent to the entire  $H\beta$  profile in Pop. A sources. We note that the decomposition  $H\beta_{\text{BC}} - H\beta_{\text{VBC}}$  of Pop. B sources assumes two Gaussians while the intrinsic shapes of  $H\beta_{\text{BC}}$  and  $H\beta_{\text{VBC}}$ , especially in the radial velocity range where they overlap is, unknown. The origin of the redward asymmetry often seen in the  $H\beta$  profile is also unclear. It seems too large to be due to grav-

itational redshift associated with line emission from increasingly smaller distances from the central black hole (under the assumption that the motion is predominantly virial). A likely possibility is non-virial motion associated with gas infall toward the central black hole (see e.g. Hu et al., 2008a; Gaskell & Goosmann, 2008, who provide renewed support for the hypothesis of infalling emitting regions), but alternatives like Compton scattering have also been considered (e.g. Kallman & Krolik, 1986). However, if the VBLR is mainly made of optically thick gas the radial velocity range underlying the  $H\beta_{BC}$  is especially ambiguous. Note also that the width reestimation is not the same as using the 2<sup>nd</sup> moment of the  $H\beta$  profile:  $\sigma$  (Peterson et al., 2004; Collin et al., 2006) may have little meaning for a composite line since it is measured on the whole  $H\beta$  profile. The reestimation leads to a more extreme reduction than suggested in Paper II; actually, all VBLR corrected FWHM values decrease to within  $1000 \text{ km s}^{-1}$  of the Pop. A-B boundary ( $4\text{--}5000 \text{ km s}^{-1}$ ). In fact the highest luminosity bins show FWHM( $H\beta_{BC}$ ) within the revised Pop. A range as defined in Figure 10.

An important implication of this correction involves its effect on  $M_{BH}$  and  $L_{Edd}$  estimation for Pop. B sources. Pop. B sources would essentially cease to exist as a separate population in the context of  $M_{BH}$  estimation. All  $M_{BH}$  values for Pop B would decrease from the previous range (Paper II)  $\log M_{BH} = 7.5 - 9.5$  to  $7.0 - 9.0$  which is more similar to the Pop. A range but still consistent with the view (Sulentic et al., 2000a) that Pop. B quasars are radiating at lower  $L_{bol}/L_{Edd}$ , as further discussed below.

Considering the uncertain and somewhat speculative nature of the corrections applied to Pop. B sources, FWHM  $H\beta$  in Pop. A sources appears to provide more direct and reliable black hole mass estimates yielding a range in  $\log M_{BH} = 6.0 - 8.5$  at low  $z$  and  $9.0 - 10.0$  at  $z \gtrsim 1.0$  (see figures in Paper II). The major source of uncertainty involves the inclination correction which depends on the BLR geometry. A weak VBLR component and/or blue asymmetry are present in an uncertain number of sources which might lead to slight overestimates of  $M_{BH}$  when assuming that the virial line component is a symmetric Lorentzian. Gaussian fits to Pop. A profiles (e.g. Shen et al., 2008) lead to significant overestimates of  $M_{BH}$ . Median values from our luminosity composite profiles (assuming mean FWHM  $H\beta$  and  $L_{bol}$  for sources in that bin) show a clear luminosity correlation ranging from  $\log M_{BH} \sim 6 - 10$  for the most luminous ISAAC sources. Estimates corrected for  $H\beta$  asymmetries are slightly lower but only for the SDSS bins.

The  $L_{bol}/L_{Edd}$  values in Table 6 increase from 0.02 to  $\gtrsim 0.6$  in the highest luminosity bins of Pop. B. We remark that the  $L_{bol}/L_{Edd}$  value for the most luminous bin ( $\approx 1$ ) is especially uncertain because of the limited number of sources and of the large correction amplitude ( $\text{FWHM}(H\beta) \approx 9300 \text{ km s}^{-1}$ ;  $\text{FWM}(H\beta_{BC}) \approx 4300 \text{ km s}^{-1}$ ).  $L_{bol}/L_{Edd}$  values obtained using FWHM ( $H\beta$ ) without removing  $H\beta_{VBC}$  (Table 7) range from  $\approx 0.02$  to 0.27. Similar values are obtained if FWHM( $\text{FeII}\lambda 4570$ ) is used as a virial estimator to compute  $M_{BH}$ . The corresponding  $L_{bol}/L_{Edd}$  estimates for Pop. A luminosity composites also show an increase ranging from  $L_{bol}/L_{Edd} \approx 0.2$  (lowest luminosity) to 1.3 in the highest luminosity bin. Ranges for Pop A from Paper II were  $L_{bol}/L_{Edd} = 0.05 - 1.0$  at low  $z$  and  $0.5 - 1.0$  at  $z \gtrsim 1.0$  assuming that sources above  $L_{bol}/L_{Edd} > 1.0$  are the result of face-on orientation. The luminosity trend is expected for both Pop. A and B since we are sampling preferentially higher  $L_{bol}/L_{Edd}$  radiators with increasing  $L_{bol}$  (as shown in Paper II). Without  $H\beta_{VBC}$  correction the difference between the  $L_{bol}/L_{Edd}$  of Pop. A and B is  $\Delta \log L_{bol}/L_{Edd} \approx 0.6$  for the SDSS luminosity bin, decreasing to  $\approx 0.3$  for the ISAAC luminosity bins (47 and 48). If we con-

sider the width of  $H\beta_{BC}$  only,  $\Delta \log L_{bol}/L_{Edd} \approx 0.5$ , even if this difference becomes rather small in the ISAAC bins, probably because of the extreme amplitude of the correction, and of the caveats listed at the beginning of this section. At any rate, from the SDSS sample we can conclude that Pop. B appears to be a population of lower Eddington ratio than Pop. A. Pop. B is likely to be an older and more evolved quasar population than Pop. A, since black holes seem to reside in hosts with large spheroidal components, often elliptical galaxies (Woo et al., 2005). On the contrary the morphology of NLSy1 hosts (i.e., in many ways the “extreme Pop. A” sources) in the local Universe often involves high surface brightness star-forming galaxies (Krongold et al., 2001; Ohta et al., 2007). They are often barred and/or remarkably perturbed suggesting that they may be young systems sustained by a large flow of matter toward their central black holes (see e.g. the review by Sulentic et al., 2008).

### 5.5. Occupation of Spectral Type B2

ISAAC sources are found in the B2 bin of the 4DE1 optical plane ( $\text{FWHM} = 4\text{--}8000 \text{ km s}^{-1}$  and  $R_{\text{FeII}} = 0.5 - 1.0$ ). The low  $z$  ATLAS sample included only 11 sources ( $\sim 5\%$ ) in that bin but the more complete SDSS sample involves 40 B2 sources ( $\sim 10\%$ ). Bin B2 may involve sources with the largest black hole masses (several times  $10^9 M_{\odot}$ ). The largest masses are expected to fall in the region of bin B2 (Zamanov & Marziani, 2002) but such massive black holes are not observed at low  $z$  (see, for example the  $M_{BH}$  distribution as a function of  $z$  in Paper II). In the ISAAC sample we derive  $M_{BH}$  values as high as  $\log M_{BH} \approx 9.7$  (Sulentic et al., 2006). According to the grid in Fig. 2 of Zamanov & Marziani (2002) the B2 bin is expected to be occupied by sources with  $M_{BH} \sim 5 \times 10^9 M_{\odot}$ . The expected  $L_{bol}/M_{BH}$  ratio is modest with  $L_{bol}/L_{Edd} \sim 0.16$ . B2 sources therefore expected to share physical properties that are thought to be typical of Pop. B. The  $H\beta$  line profile is well described by a double Gaussian decomposition also if we restrict our attention to revised bin MB2. This result is consistent with the conclusion that most sources in bin B2 are similar to those in B1 although with stronger  $R_{\text{FeII}}$ . The  $H\beta$  line profiles imply that both types may fall on the Pop. B side of a critical  $L_{bol}/L_{Edd}$  that separates Pop. A and Pop. B boundary.

## 6. Conclusions

We presented VLT-ISAAC spectroscopic observations for 30 intermediate  $z$  and high-luminosity HE quasars. Combined with previous data we have a sample of 53 objects ( $z = 0.9 - 3.0$ ) which we compare with two large low- $z$  samples (Marziani et al., 2003a; Zamfir et al., 2008). We find few correlations/trends between broad emission line properties and source luminosity. We previously proposed an empirical limit at  $\text{FWHM}(H\beta) \approx 4000 \text{ km s}^{-1}$  to distinguish between two populations A-B of quasars with very different spectroscopic properties. Sources with  $\text{FWHM}(H\beta) < 4000 \text{ km s}^{-1}$  show Lorentzian  $H\beta$  profiles while those above this limit are best fit with double Gaussian models. This low  $z$ / low luminosity dichotomy is also found for the high luminosity ISAAC sources. Elementary  $L_{bol}/L_{Edd}$  computations suggest that the dichotomy may be explained if a critical  $L_{bol}/L_{Edd}$  is associated with a BLR structure change, but the issue of the Pop. A/B boundary deserves further scrutiny. Once the population A/B dichotomy is taken into account the phenomenology of the  $H\beta_{BC}$  emitting region, as well as inferences about BLR structure are quite similar over a 5 dex luminosity range that includes some of the most luminous known

quasars. This overall scenario is described in more detail by the following results of the present paper:

1. A minimum requirement for quantifying and interpreting BLR properties in Type 1 AGN involves the Pop. A–B dichotomy. Spectroscopic averaging without such a discrimination appears to be equivalent to discussing stellar properties without consideration of the OBAFGKM spectroscopic sequence
2. Pop. A sources show a minimum FWHM  $H\beta$  that increases with source luminosity from  $\sim 500$ – $1000 \text{ km s}^{-1}$  to  $3000$ – $3500 \text{ km s}^{-1}$ . The best boundary to this lower envelope favors an exponent  $\lesssim 0.67$  in the Kaspi relation. Pop. A sources span a FWHM  $H\beta$  range of  $\sim 4000 \text{ km s}^{-1}$  driven by source orientation and virial motions in an accretion disk. The virial assumption implies a  $M_{\text{BH}}$  range of 4dex ( $\log M_{\text{BH}} = 6$ – $10$ ) for this high accreting population. In the ISAAC sample studied in this paper Pop. A sources show  $-0.7 \lesssim \log L_{\text{bol}}/L_{\text{Edd}} \lesssim 0.18$ .
3.  $H\beta$  emission in Pop. B sources involves both unshifted broad ( $H\beta_{\text{BC}}$ ) and redshifted very broad line ( $H\beta_{\text{VBC}}$ ) components. Pop. B shows a “super” Baldwin effect with  $W(H\beta_{\text{BC}})$  decreasing by a factor 4 with increasing  $L_{\text{bol}}$ . At the same time  $W(H\beta_{\text{VBC}})$  remains almost constant implying that it arises in a photo-ionized optically thick medium. FWHM( $H\beta_{\text{BC}}$ ) component shows no luminosity dependence after correction for  $H\beta_{\text{VBC}}$  broadening. This yields an  $M_{\text{BH}}$  range similar to that for Pop. A. Pop. B is a lower accreting population with  $-1.1 \lesssim \log L_{\text{bol}}/L_{\text{Edd}} \lesssim -0.2$  for the objects of this paper. One should bear in mind the caveats of §4.6 in analyzing the  $L_{\text{bol}}/L_{\text{Edd}}$  limits, and that 80% of Pop. B sources of the ISAAC sample show  $\log L_{\text{bol}}/L_{\text{Edd}} \lesssim -0.4$ . Considering the blurring by errors in  $L_{\text{bol}}/L_{\text{Edd}}$  estimates, and results of previous papers, intrinsic  $L_{\text{bol}}/L_{\text{Edd}}$  ranges could be  $\approx 0.01$  –  $0.2$  (Pop. B) and  $\approx 0.2$  –  $1$  (Pop. A), with a separation at  $L_{\text{bol}}/L_{\text{Edd}} \approx 0.2 \pm 0.1$ . Pop. B sources in the SDSS sample seem to remain a population of lower Eddington ratio even if the extreme correction to FWHM implied by removal of the  $H\beta_{\text{VBC}}$  is applied (§5.4).
4. Most Type 1 AGN do not show broad line profiles consistent with simple accretion disk models. Perhaps Lorentzian Pop. A profiles can be accommodated with thin/slim disk emission models (if disk emission is very extended) but Pop. B cannot. The redshifted  $H\beta_{\text{VBC}}$  in Pop. B sources can not be considered part of a double peak signature since the asymmetry and the centroid shift at  $\frac{1}{4}$  intensity (near the profile base is usually too large to be attributed to a gravitational redshift. Arp 102B – the prototypical “double-peaked” Balmer line emitter – shows a redshift at line base that is modest, and consistent with the value expected for gravitational redshift at the inner emitting radius of the accretion disk according to the model of Chen et al. (1989). This is however not the case for many Pop. B objects that have been included in so-called double-peaked source compilations (i.e. as accretion disk candidates: e.g., Strateva et al., 2003).
5.  $H\beta_{\text{VBC}}$  is the dominant broad line component at high luminosity (from  $\sim 25\%$  to  $60\%$  of the  $H\beta$  flux over our  $L_{\text{bol}}$  range) for Pop. B sources. The geometry and kinematics of the VBLR are yet unclear. The  $H\beta_{\text{VBC}}$  redshift  $\Delta v \approx 1$ – $2000 \text{ km s}^{-1}$  is unlikely to be gravitational in nature. The increase in dominance with redshift favors a connection to the hypothesized infall involved with the  $M_{\text{BH}}$  growth. Another

possibility involves photon downshifting via some form of scattering (e.g. Laor, 2006, and references therein).

*Acknowledgements.* Funding for the SDSS and SDSS-II has been provided by the Alfred P. Sloan Foundation, the Participating Institutions, the National Science Foundation, the U.S. Department of Energy, the National Aeronautics and Space Administration, the Japanese Monbukagakusho, the Max Planck Society, and the Higher Education Funding Council for England. The SDSS Web Site is <http://www.sdss.org/>. The SDSS is managed by the Astrophysical Research Consortium for the Participating Institutions. The Participating Institutions are the American Museum of Natural History, Astrophysical Institute Potsdam, University of Basel, University of Cambridge, Case Western Reserve University, University of Chicago, Drexel University, Fermilab, the Institute for Advanced Study, the Japan Participation Group, Johns Hopkins University, the Joint Institute for Nuclear Astrophysics, the Kavli Institute for Particle Astrophysics and Cosmology, the Korean Scientist Group, the Chinese Academy of Sciences (LAMOST), Los Alamos National Laboratory, the Max-Planck-Institute for Astronomy (MPIA), the Max-Planck-Institute for Astrophysics (MPA), New Mexico State University, Ohio State University, University of Pittsburgh, University of Portsmouth, Princeton University, the United States Naval Observatory, and the University of Washington.

## References

- Aoki, K., Kawaguchi, T., & Ohta, K. 2005, *ApJ*618, 601
- Bachev, R., Marziani, P., Sulentic, J. W., Zamanov, R., Calvani, M., & Dultzin-Hacyan, D. 2004, *ApJ*, 617, 171
- Baker, A. C., Carswell, R. F., Bailey, J. A., Espey, B. R., Smith, M. G., & Ward, M. J. 1994, *MNRAS*, 270, 575
- Baldwin, J. A., Burke, W. L., Gaskell, C. M., & Wampler, E. J. 1978, *Nature*, 273, 431
- Baskin, A., & Laor, A. 2005, *MNRAS*, 356, 1029
- Bentz, M. C., Peterson, B. M., Pogge, R. W., Vestergaard, M., & Onken, C. A. 2006, *ApJ*, 644, 133
- Blaes, O. 2007, *The Central Engine of Active Galactic Nuclei*, 373, 75
- Bock, D. C.-J., Large, M. I., & Sadler, E. M. 1999, *AJ*, 117, 1578
- Bonning, E. W., Cheng, L., Shields, G. A., Salviander, S., & Gebhardt, K. 2007, *ApJ*, 659, 211
- Boroson, T. A. 2002, *ApJ*, 565, 78
- Boroson, T. 2005, *AJ*, 130, 381
- Boroson, T. A., & Green, R. F. 1992, *ApJS*, 80, 109
- Brinkmann, W., Grupe, D., Branduardi-Raymont, G., & Ferrero, E. 2003, *A&A*, 398, 81
- Brotherton, M. S., Wills, B. J., Steidel, C. C., & Sargent, W. L. W. 1994, *ApJ*, 423, 131
- Bruhweiler, F., & Verner, E. 2008, *ApJ*, 675, 83
- Carswell, R. F., et al. 1991, *ApJ*, 381, L5
- Chen, K., Halpern, J. P., & Filippenko, A. V. 1989, *ApJ*, 339, 742
- Collin, S., Kawaguchi, T., Peterson, B. M., & Vestergaard, M. 2006, *A&A*, 456, 75
- Collin-Souffrin, S., Dyson, J. E., McDowell, J. C., & Perry, J. J. 1988, *MNRAS*, 232, 539
- Corbin, M. R. 1995, *ApJ*, 447, 496
- Corbin, M. R., & Smith, P. S. 2000, *ApJ*, 532, 136
- Elston, R., Thompson, K. L., & Hill, G. J. 1994, *Nature*, 367, 250
- Eracleous, M., & Halpern, J. P. 2003, *ApJ*, 599, 886
- Espey, B. R., Carswell, R. F., Bailey, J. A., Smith, M. G., & Ward, M. J. 1989, *ApJ*, 342, 666
- Evans, A. S., Sanders, D. B., Cutri, R. M., Radford, S. J. E., Surace, J. A., Solomon, P. M., Downes, D., & Kramer, C. 1998, *ApJ*, 506, 205
- Ferland, G. J., Korista, K. T., Verner, D. A., Ferguson, J. W., Kingdon, J. B., & Verner, E. M. 1998, *PASP*, 110, 761
- Fine, S., et al. 2008, *ArXiv e-prints*, 807, arXiv:0807.1155
- Hill, G. J., Thompson, K. L., & Elston, R. 1993, *ApJ*, 414, L1
- Gaskell, C. M. 1985, *ApJ*, 325, 114
- Gaskell, C. M., & Goosmann, R. W. 2008, arXiv:0805.4258
- Hopkins, P. F., Richards, G. T., & Hernquist, L. 2007, *ApJ*, 654, 731
- Hu, C., Wang, J.-M., Ho, L. C., Bian, W.-H., & Xue, S.-J. 2008b, *ApJ*, 683, L11
- Hu, C., Wang, J.-M., Ho, L. C., Chen, Y.-M., Zhang, H.-T., Bian, W.-H., & Xue, S.-J. 2008a, *ApJ*, 687, 78
- Hubeny, I., Agol, E., Blaes, O., & Krolik, J. H. 2000, *ApJ*, 533, 710
- Kallman, T. R., & Krolik, J. H. 1986, *ApJ*, 308, 805
- Kaspi, S., Smith, P. S., Netzer, H., Maoz, D., Jannuzi, B. T., & Giveon, U. 2000, *ApJ*, 533, 631
- Kaspi, S., Maoz, D., Netzer, H., Peterson, B. M., Vestergaard, M., & Jannuzi, B. T. 2005, *ApJ*, 629, 61
- Kelly, B. C., Bechtold, J., Trump, J. R., Vestergaard, M., & Siemiginowska, A. 2008, *ArXiv e-prints*, 801, arXiv:0801.2383
- Komossa, S., Xu, D., Zhou, H., Storchi-Bergmann, T., & Binette, L. 2008, *ApJ*, 680, 926
- Krongold, Y., Dultzin-Hacyan, D., & Marziani, P. 2001, *AJ*, 121, 702
- Kuhr, H., McAlary, C. W., Rudy, R. J., Strittmatter, P. A., & Rieke, G. H. 1984, *ApJ*, 284, L5
- Laor, A. 2006, *ApJ*, 643, 112
- Marconi, A., Axon, D. J., Maiolino, R., Nagao, T., Pastorini, G., Pietrini, P., Robinson, A., & Torricelli, G. 2008, *ApJ*, 678, 693
- Marziani, P., Dultzin, D., & Sulentic, J. W. 2008, *Revista Mexicana de Astronomia y Astrofisica Conference Series*, 32, 103
- Marziani, P., Sulentic, J. W., Dultzin-Hacyan, D., Calvani, M., & Moles, M. 1996, *ApJS*, 104, 37
- Marziani, P., Sulentic, J. W., Zamanov, R., Calvani, M., Dultzin-Hacyan, D., Bachev, R., & Zwitter, T. 2003a, *ApJS*, 145, 199
- Marziani P., Zamanov R., Sulentic J. W., Calvani M., 2003b, *MNRAS*, 345, 1133
- Murayama, T., Taniguchi, Y., Evans, A. S., Sanders, D. B., Hodapp, K.-W., Kawara, K., & Arimoto, N. 1999, *AJ*, 117, 1645
- Murayama, T., Taniguchi, Y., Evans, A. S., Sanders, D. B., Ohya, Y., Kawara, K., & Arimoto, N. 1998, *AJ*, 115, 2237
- Nazarova, L. S., Bochkarev, N. G., & O'Brien, P. T. 2007, *Astronomical and Astrophysical Transactions*, 26, 401
- Netzer, H. 1990, in Blandford, R. D., Netzer, H., Woltjer, L., Courvoisier, T. J.-L., & Mayor, M. (eds.) in *Active Galactic Nuclei*, Saas-Fee Advanced Course 20. Lecture Notes 1990. Swiss Society for Astrophysics and Astronomy, XII, Springer-Verlag: Berlin Heidelberg New York
- Netzer, H., Lira, P., Trakhtenbrot, B., Shemmer, O., & Cury, I. 2007, *ApJ*, 671, 1256
- Netzer, H., & Trakhtenbrot, B. 2007, *ApJ*, 654, 754
- Ohta, K., Aoki, K., Kawaguchi, T., & Kiuchi, G. 2007, *ApJS*, 169, 1
- Osterbrock, D. E., & Pogge, R. W. 1985, *ApJ*, 297, 166
- Peterson, B. M., et al. 2004, *ApJ*, 613, 682
- Reimers, D., Koehler, T., & Wisotzki, L. 1996, *AApS*, 115, 235
- Rokaki, E., Lawrence, A., Economou, F., & Mastichiadis, A. 2003, *MNRAS*, 340, 1298
- Shang, Z., Wills, B. J., Robinson, E. L., Wills, D., Laor, A., Xie, B., & Yuan, J. 2003, *ApJ*, 586, 52
- Shang, Z., Wills, B. J., Wills, D., & Brotherton, M. S. 2007, *AJ*, 134, 294
- Shen, Y., Greene, J. E., Strauss, M. A., Richards, G. T., & Schneider, D. P. 2008, *ApJ*, 680, 169
- Sigut, T. A. A., Pradhan, A. K., & Nahar, S. N. 2004, *ApJ*, 611, 81
- Sigut, T. A. A., & Pradhan, A. K. 2003, *ApJS*, 145, 15
- Strateva, I. V., et al. 2003, *AJ*, 126, 1720
- Sulentic, J. W., Bachev, R., Marziani, P., Negrete, C. A., & Dultzin, D. 2007, *ApJ*, 666, 757
- Sulentic, J. W., Marziani, P., & Dultzin-Hacyan, D. 2000a, *ARA&A*, 38, 521
- Sulentic, J. W., Marziani, P., Zwitter, T., Dultzin-Hacyan, D., & Calvani, M. 2000b, *ApJ*, 536, L5
- Sulentic, J. W., Marziani, P., Zwitter, T., Dultzin-Hacyan, D., & Calvani, M. 2000c, *ApJ*, 545, L15
- Sulentic, J. W., Marziani, P., Zamanov, R., Bachev, R., Calvani, M., & Dultzin-Hacyan, D. 2002, *ApJ*, 566, L71
- Sulentic, J. W., Zamfir, S., Marziani, P., & Dultzin, D. 2008, *Revista Mexicana de Astronomia y Astrofisica Conference Series*, 32, 51
- Sulentic, J. W., Repetto, P., Stirpe, G. M., Marziani, P., Dultzin-Hacyan, D., & Calvani, M. 2006, *AAp*, 456, 929 (Paper II)
- Sulentic, J. W., Stirpe, G. M., Marziani, P., Zamanov, R., Calvani, M., & Braitto, V. 2004, *AAp*, 423, 121 (Paper I)
- Sulentic, J. W., Zamfir, S., Marziani, P., Bachev, R., Calvani, M., Dultzin-Hacyan, D., 2003, *ApJ*, 597, L17
- Tsuzuki, Y., Kawara, K., Yoshii, Y., Oyabu, S., Tanabé, T., & Matsuoka, Y. 2006, *ApJ*, 650, 57
- Verner, E. M., Verner, D. A., Korista, K. T., Ferguson, J. W., Hamann, F., & Ferland, G. J. 1999, *ApJS*, 120, 101
- Véron-Cetty, M.-P., Joly, M., & Véron, P. 2004, *A&A*, 417, 515
- Vestergaard, M., & Peterson, B. M. 2006, *ApJ*, 641, 689
- Wisotzki, L., Christlieb, N., Bade, N., Beckmann, V., Köhler, T., Vanelle, C., & Reimers, D. 2000, *A&A*, 358, 77
- Woo, J.-H., Urry, C. M., van der Marel, R. P., Lira, P., & Maza, J. 2005, *ApJ*, 631, 762
- Xu, Y., Bian, W.-H., Yuan, Q.-R., & Huang, K.-L. 2008, *ArXiv e-prints*, 806, arXiv:0806.1787
- Yip, C. W., et al. 2004, *AJ*, 128, 2603
- Zamanov, R., & Marziani, P. 2002, *ApJ*, 571, L77
- Zamanov, R., Marziani, P., Sulentic, J. W., Calvani, M., Dultzin-Hacyan, D., & Bachev, R. 2002, *ApJ*, 576, L9
- Zamfir, S., Sulentic, J. W., & Marziani, P. 2008, *MNRAS*, 387, 856
- Zhou, H., Wang, T., Yuan, W., Lu, H., Dong, X., Wang, J., & Lu, Y. 2006, *ApJS*, 166, 128

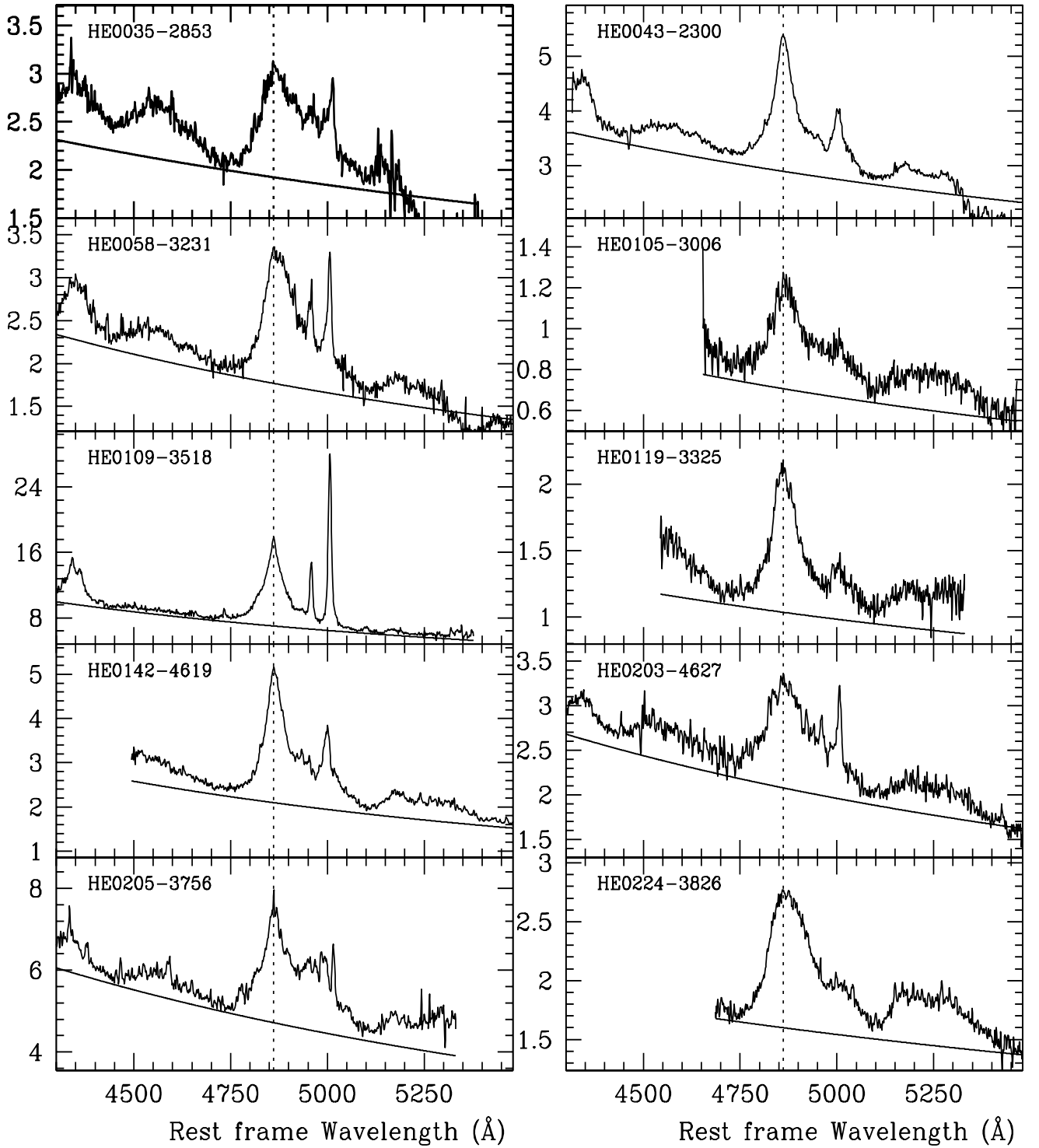


**Fig. 1.** Calibrated VLT-ISAAC spectra for 30 new intermediate-redshift quasars. Abscissæ are rest-frame wavelength in  $\text{\AA}$ , ordinates are rest-frame specific flux in units of  $10^{-15} \text{ erg s}^{-1} \text{ cm}^{-1} \text{ \AA}^{-1}$ . The spectrum behavior of HE 0035–2853, HE0043–2300, HE 0058–3231 is fully unreliable beyond  $\approx 5250 \text{ \AA}$  due to heavy atmospheric absorption also affecting the calibration standard.

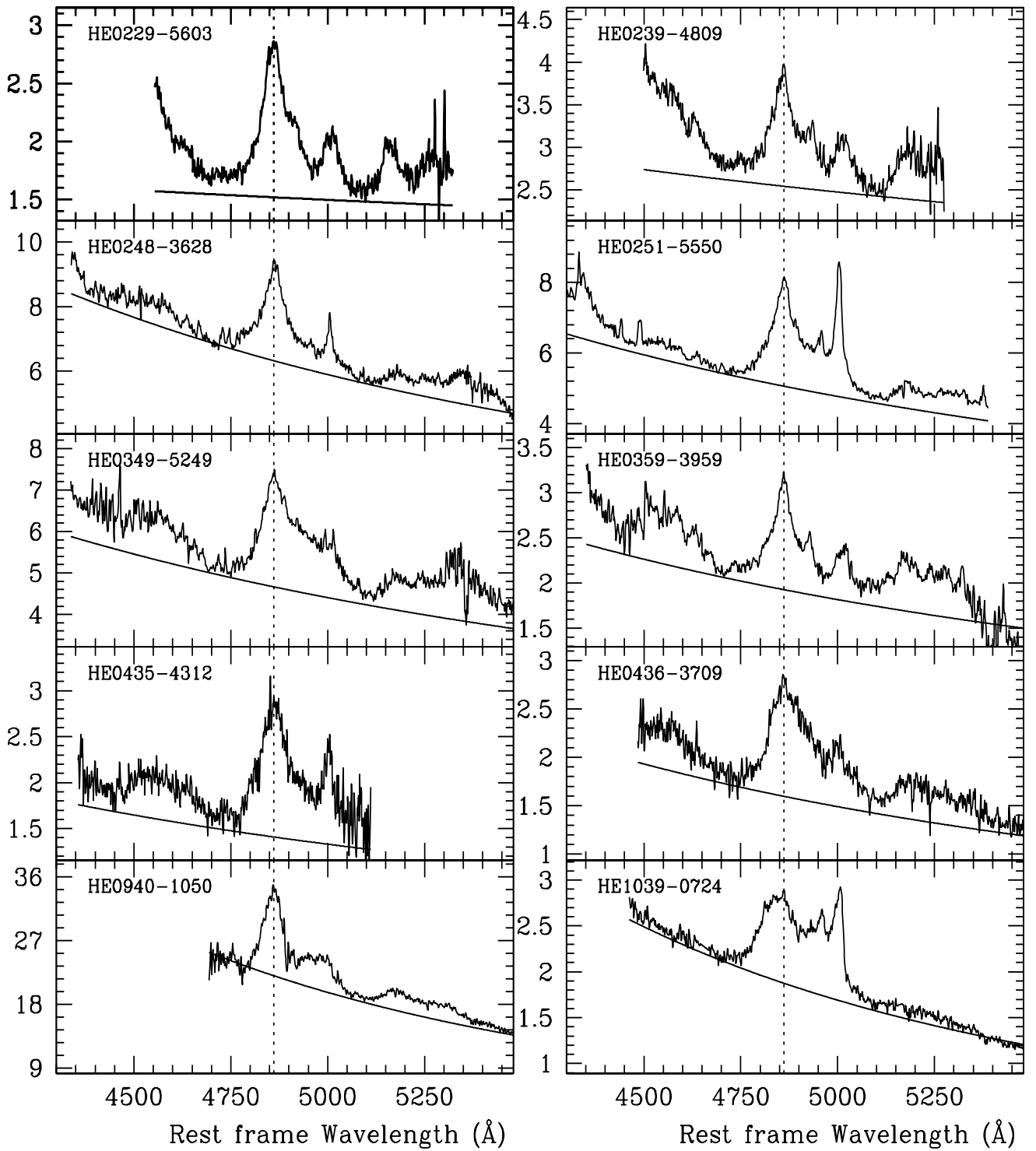


Fig. 1. Cont.

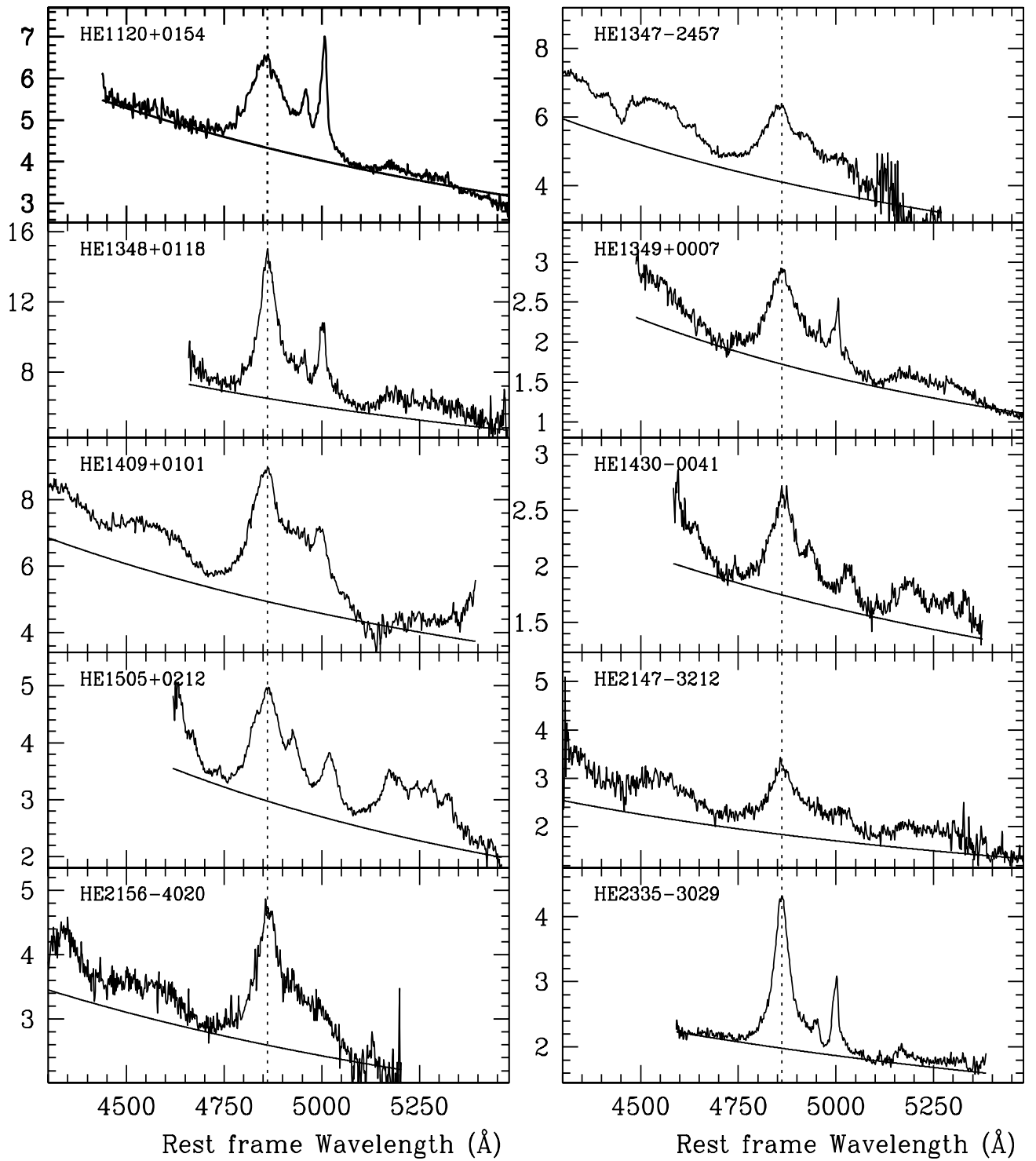
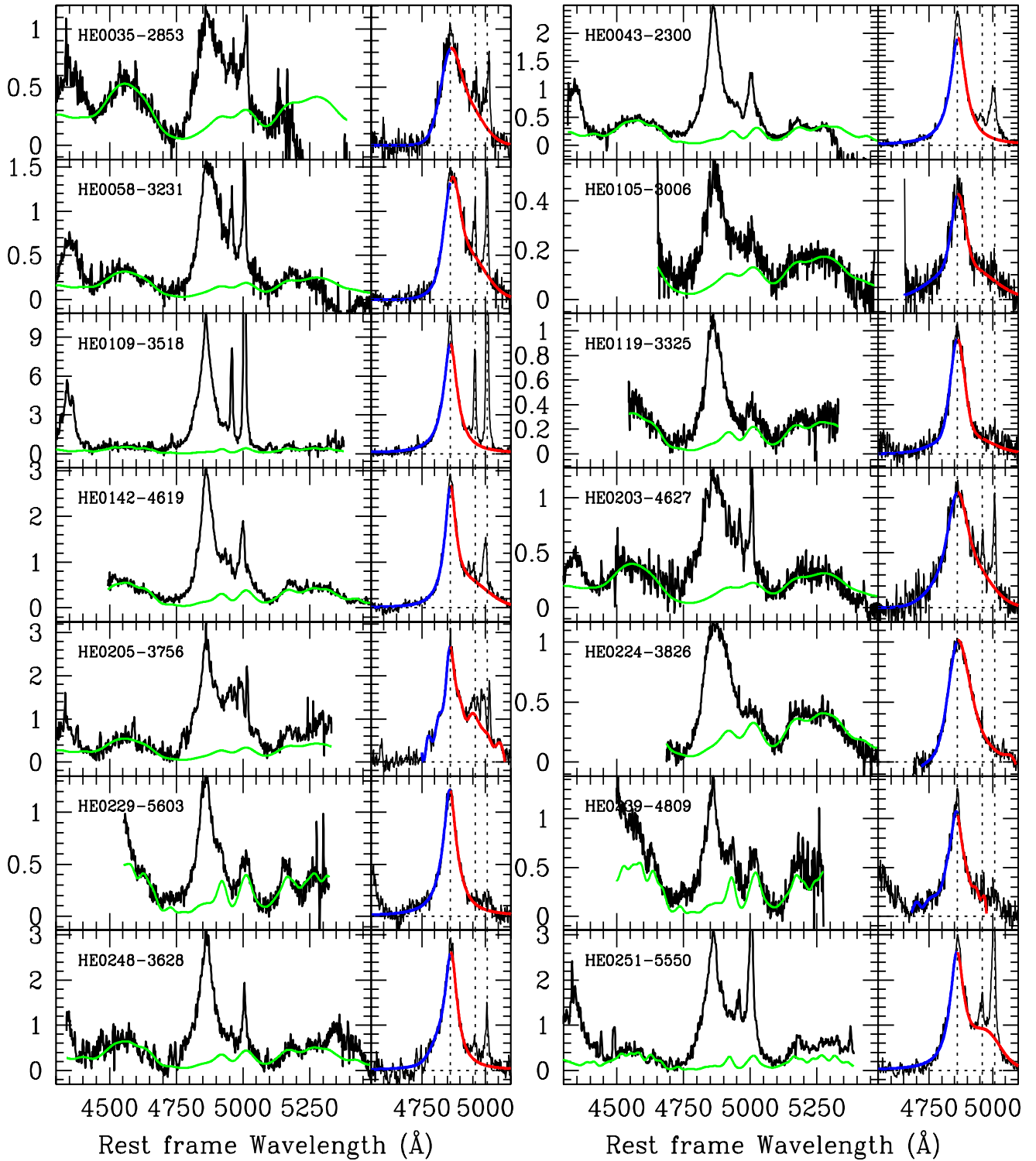


Fig. 1. Cont.



**Fig. 2.** Continuum-subtracted spectra. Left-hand panels: the  $H\beta$  spectral regions. The thin green lines show the  $FeII$  emission. Right-hand panels: spectra after continuum and  $FeII$  subtraction. The  $H\beta$  profile (broad + very broad) is marked by the thick line, blue on the short-wavelength side with respect to the rest wavelength, red on the long-wavelength side. Abscissa is rest frame wavelength in  $\text{\AA}$ , ordinate is specific flux in units of  $10^{-15} \text{ erg s}^{-1} \text{ cm}^{-2} \text{ \AA}^{-1}$ .



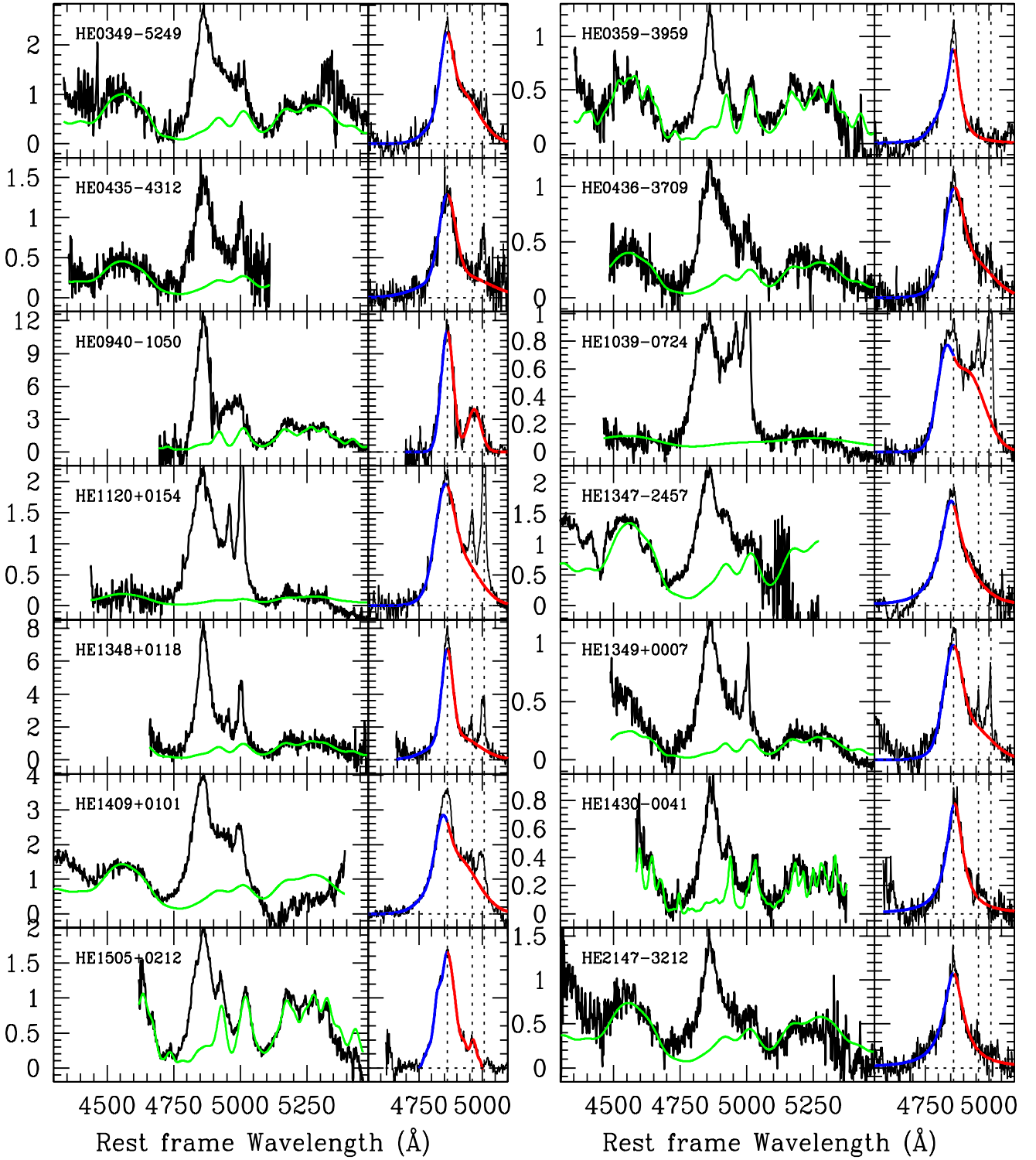


Fig. 2. Cont.

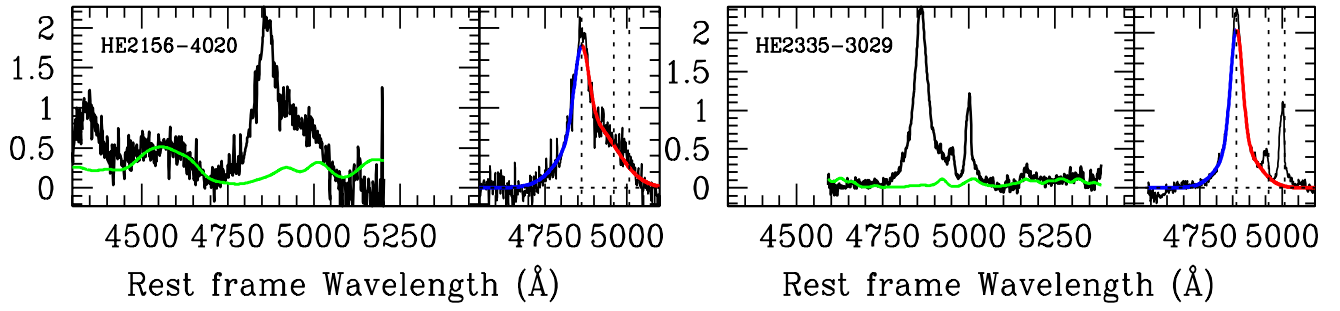
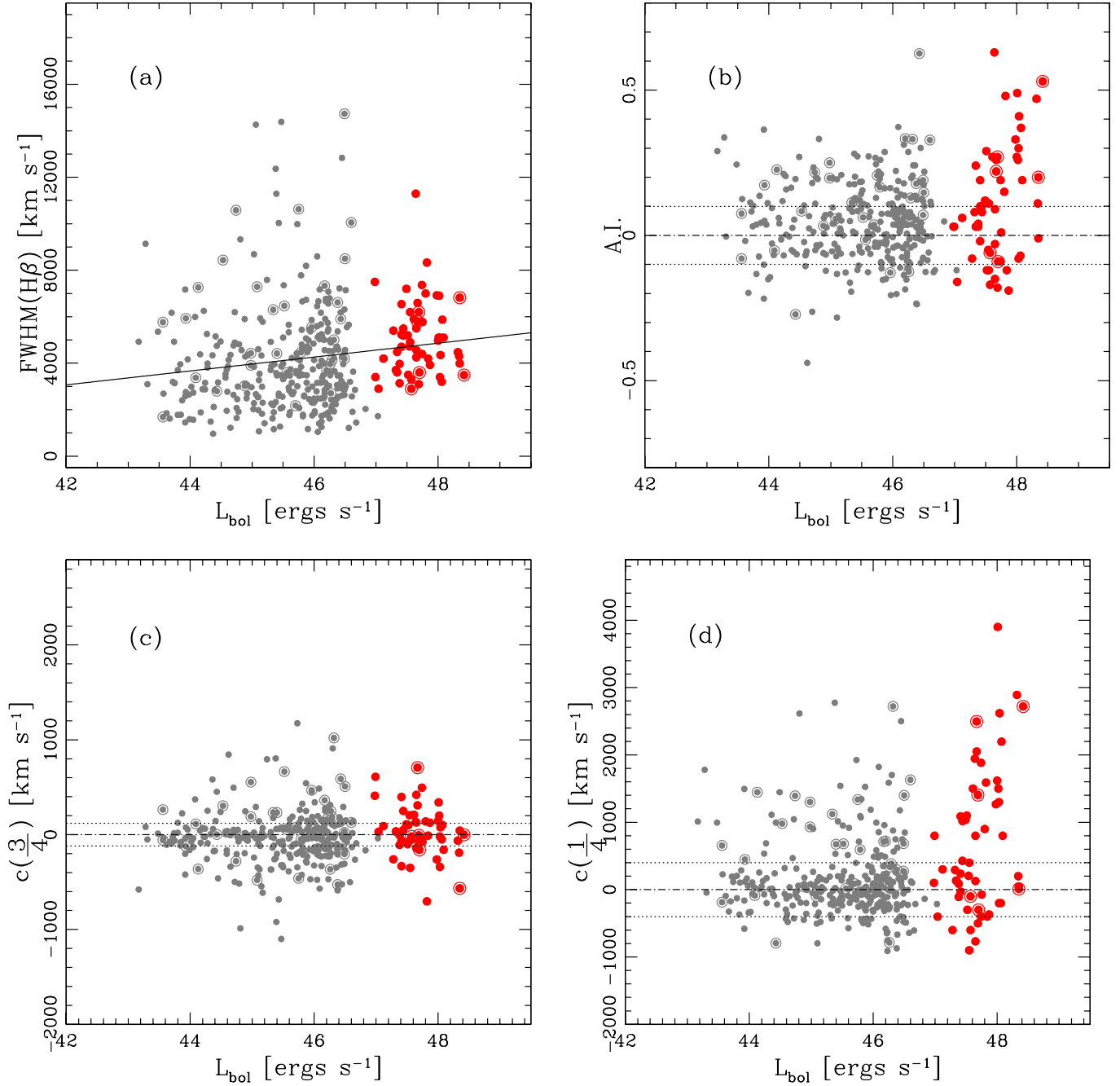
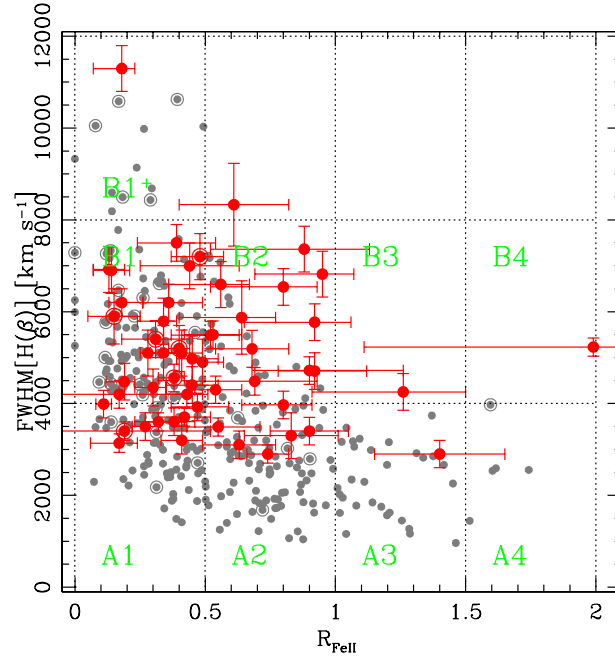


Fig. 2. Cont.



**Fig. 3.** FWHM( $H\beta$ ) in  $\text{km s}^{-1}$  (a), Asymmetry Index (b), centroid at 3/4 fractional heights, in  $\text{km s}^{-1}$  (c), and centroid at 1/4 fractional height, in  $\text{km s}^{-1}$  (d) as a function of bolometric luminosity in units of  $\text{erg s}^{-1}$ . Small gray circles: data from the SDSS sample of Zamfir et al. (2008); larger filled circles: ISAAC sample. Circled data points identify RL sources. In the upper left panel, the continuous line shows an unweighted lsq best fit. The dotted lines identify the  $\pm 2\sigma$  confidence limit for A.I., and centroids equal to zero.



**Fig. 4.** The optical plane of Eigenvector 1 with the VLT sources presented in this paper and in Paper I and II (large red filled circles), and the SDSS sample of Zamfir et al. (2008, small grey circles). Circled data points identify RL sources. Abscissa is  $FeII\lambda 4570$  prominence  $R_{FeII}$ , ordinate is  $FWHM(H\beta)$  in  $km\ s^{-1}$ . The plane is subdivided in spectral types following Sulentic et al. (2002).

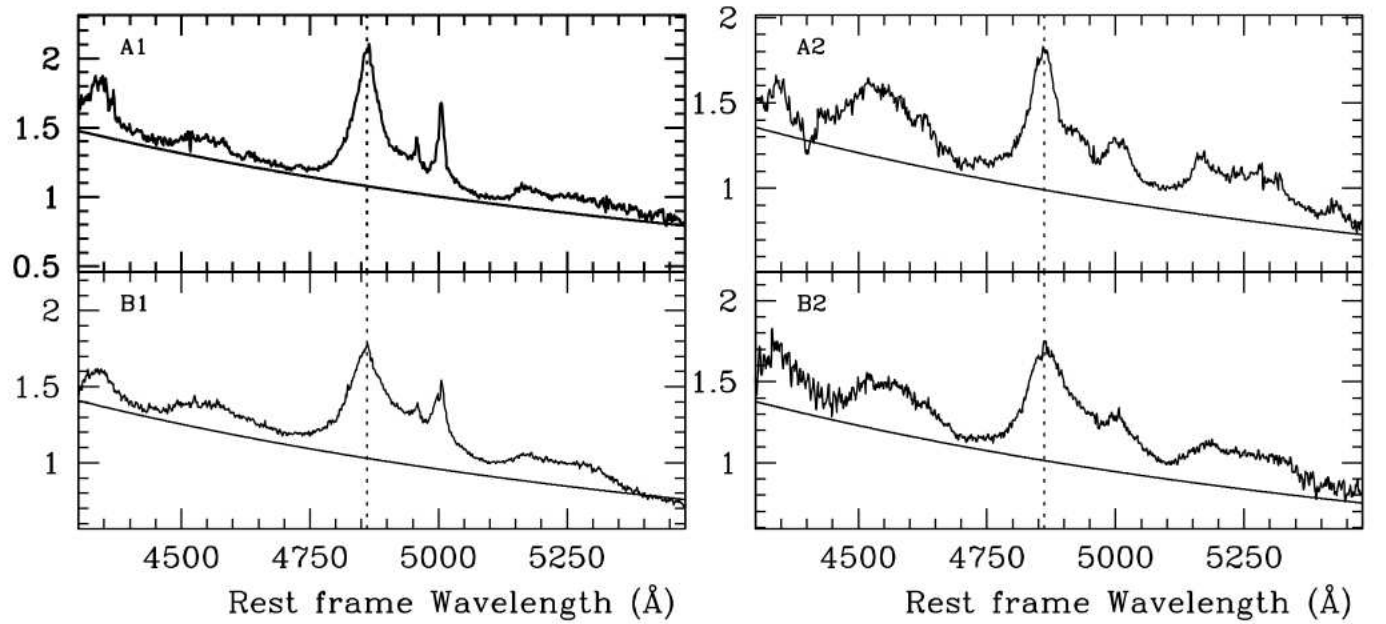


**Fig. 5.** Median spectra for bins A1, B1, A2, B2, as defined in Fig. 4. Original spectral have been normalized to unity at  $\lambda = 5100\ \text{\AA}$ . The adopted continuum is shown as a solid line.

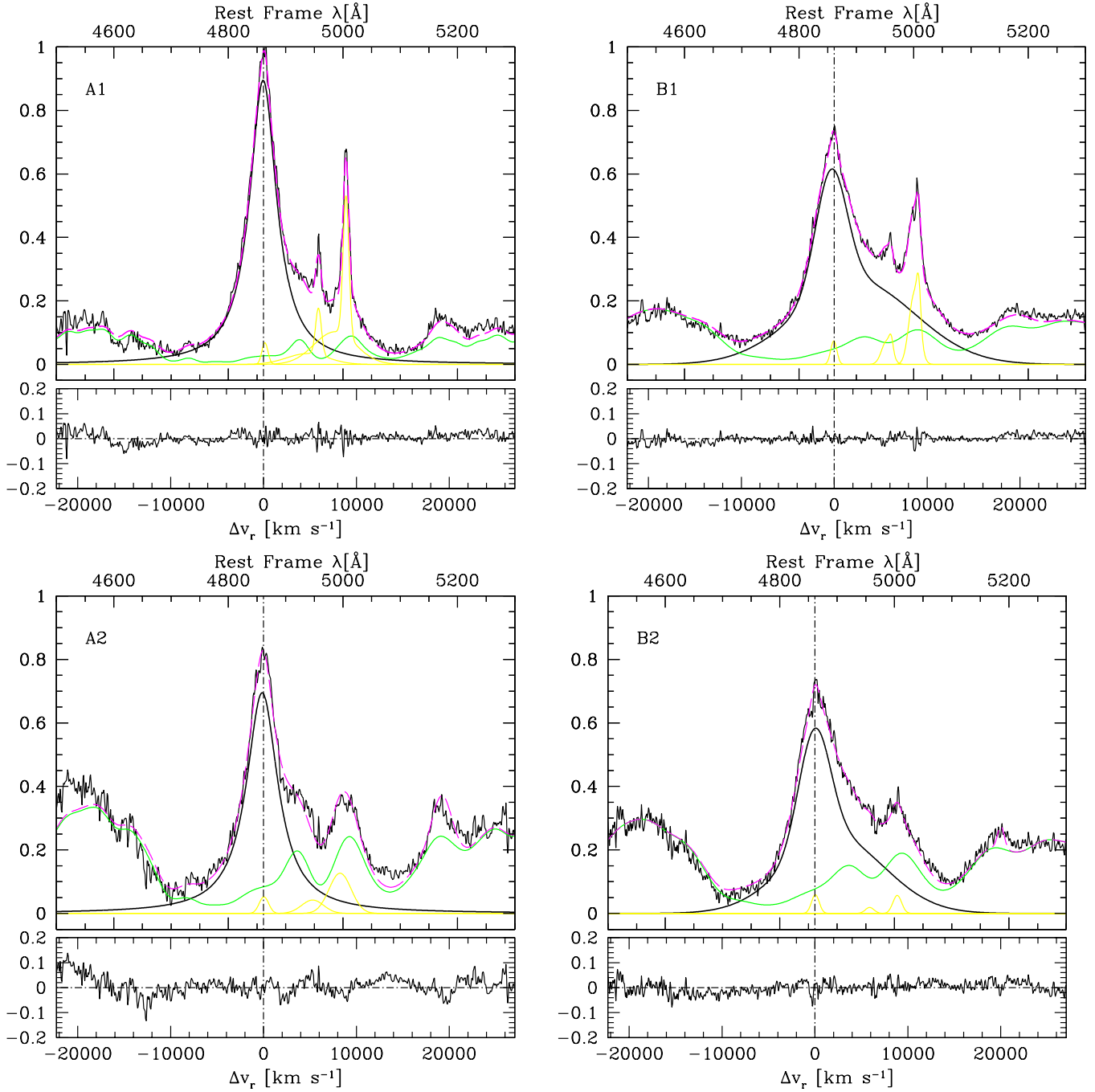


**Fig. 6.** Analysis of the  $H\beta$  profiles for spectral types A1, A2, B1, B2. Median spectra are shown after continuum subtraction (thin line); the model fit obtained with `specfit` is shown as a thick dashed magenta line. The  $H\beta$  profile is represented either by a Lorentzian function or by the sum of two Gaussians (not shown individually; thick lines). The thin green line shows the  $\text{Fe II}_{\text{opt}}$  contributions, and the yellow lines the  $[\text{O III}]\lambda\lambda 4959, 5007$  and  $H\beta_{\text{NC}}$  emission. Residuals of the fitting procedure are displayed in the window immediately below the one showing the spectral components. Abscissa scale is rest frame wavelength in  $\text{\AA}$  (top), and radial velocity in  $\text{km s}^{-1}$  from rest wavelength of  $H\beta$  (bottom).

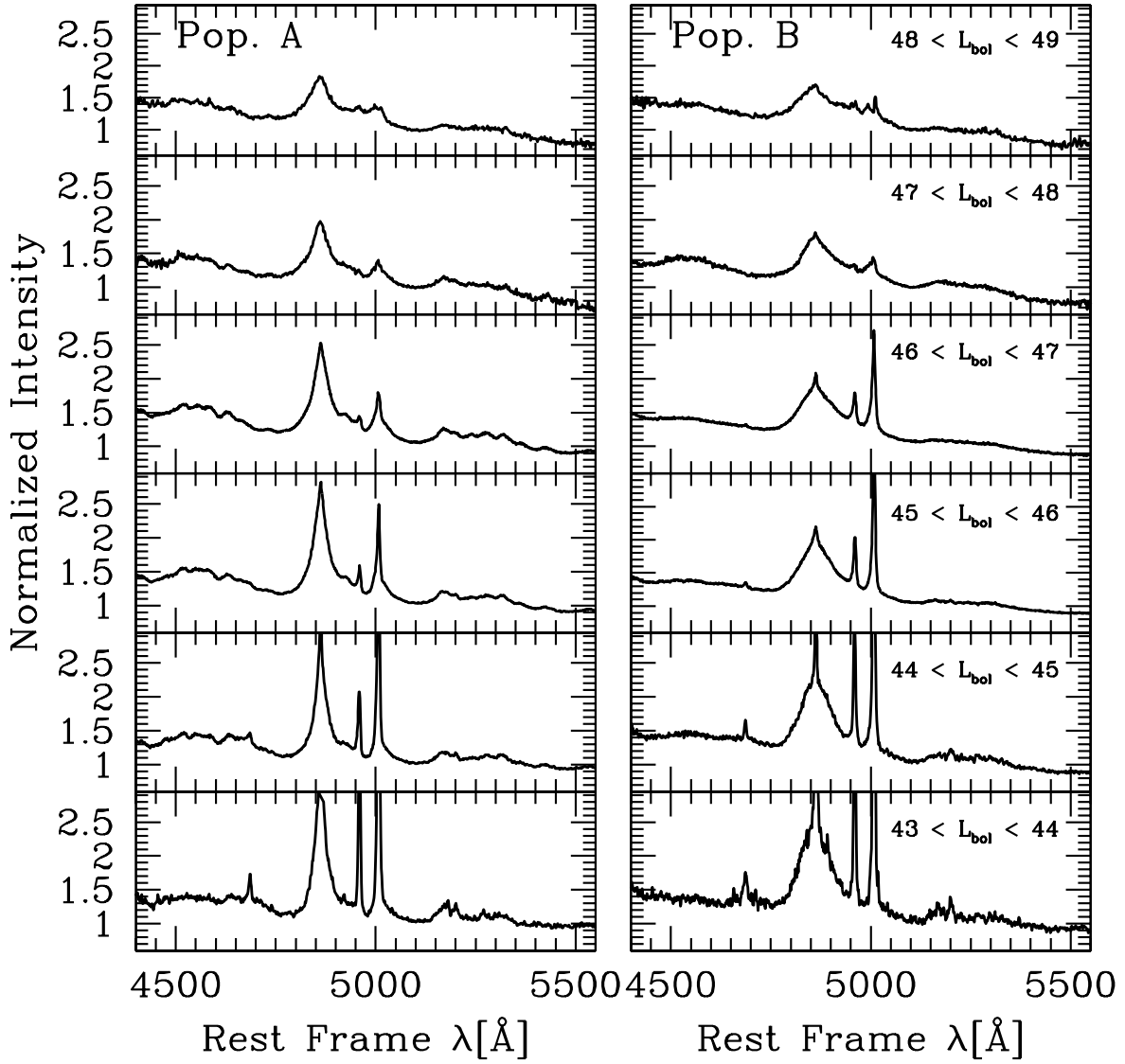


**Fig. 7.** Luminosity effects in the median spectra of Pop. A and Pop. B sources, binned in decades of luminosity in the luminosity ranges  $43 < \log L_{bol} < 49$ . Abscissa is rest frame wavelength in  $\text{\AA}$ , ordinate is normalized intensity (set to unity at  $\lambda = 5100 \text{ \AA}$ ).

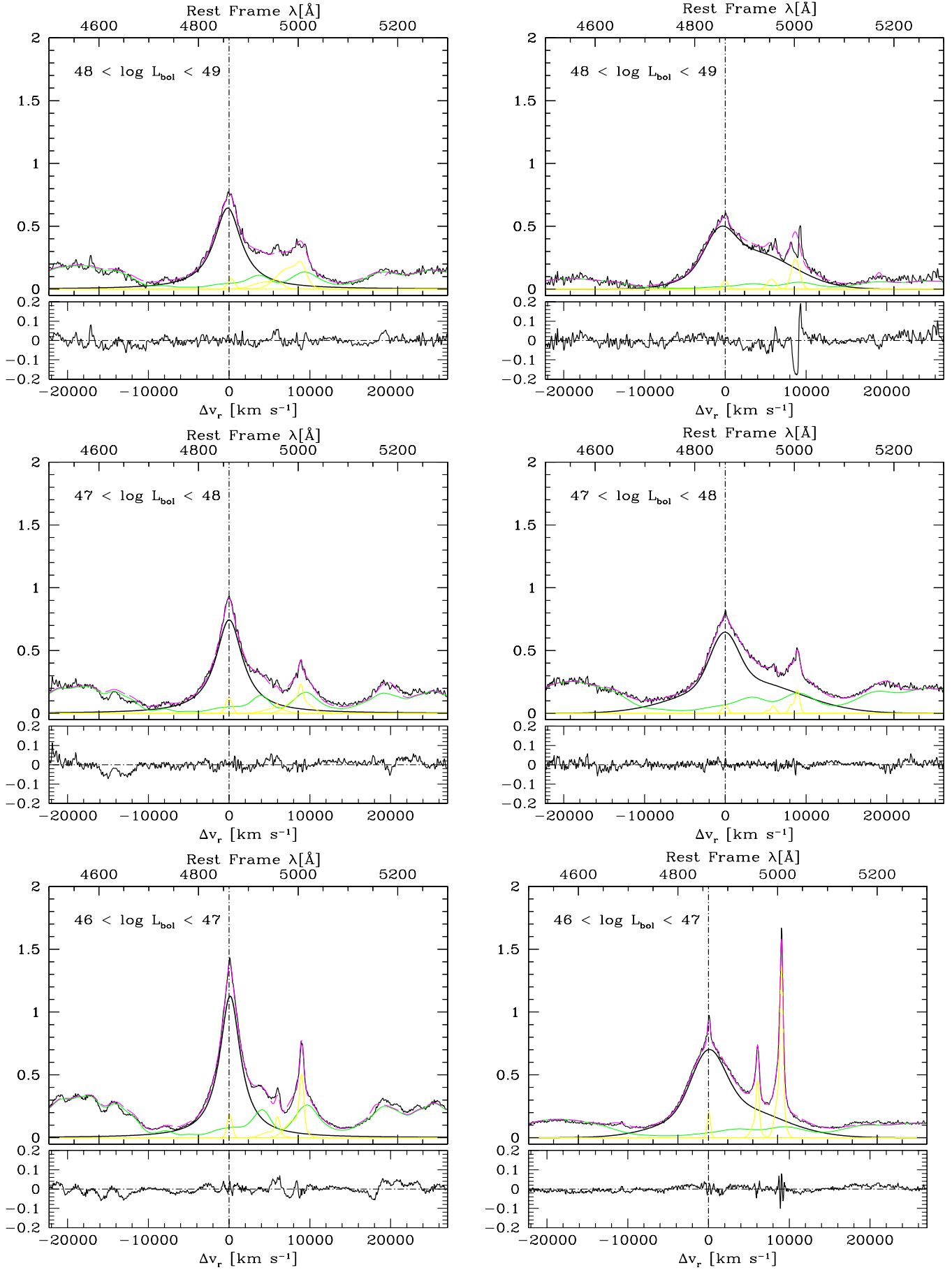


**Fig. 8.** Median spectra analysis of the  $H\beta$  profiles as a function of luminosity, for Pop. A and B (right panels). The median spectra have been continuum-subtracted. Lines follow the same coding of Fig. 6. Residuals of the fitting procedure are displayed in the window immediately below the one showing the spectral components.

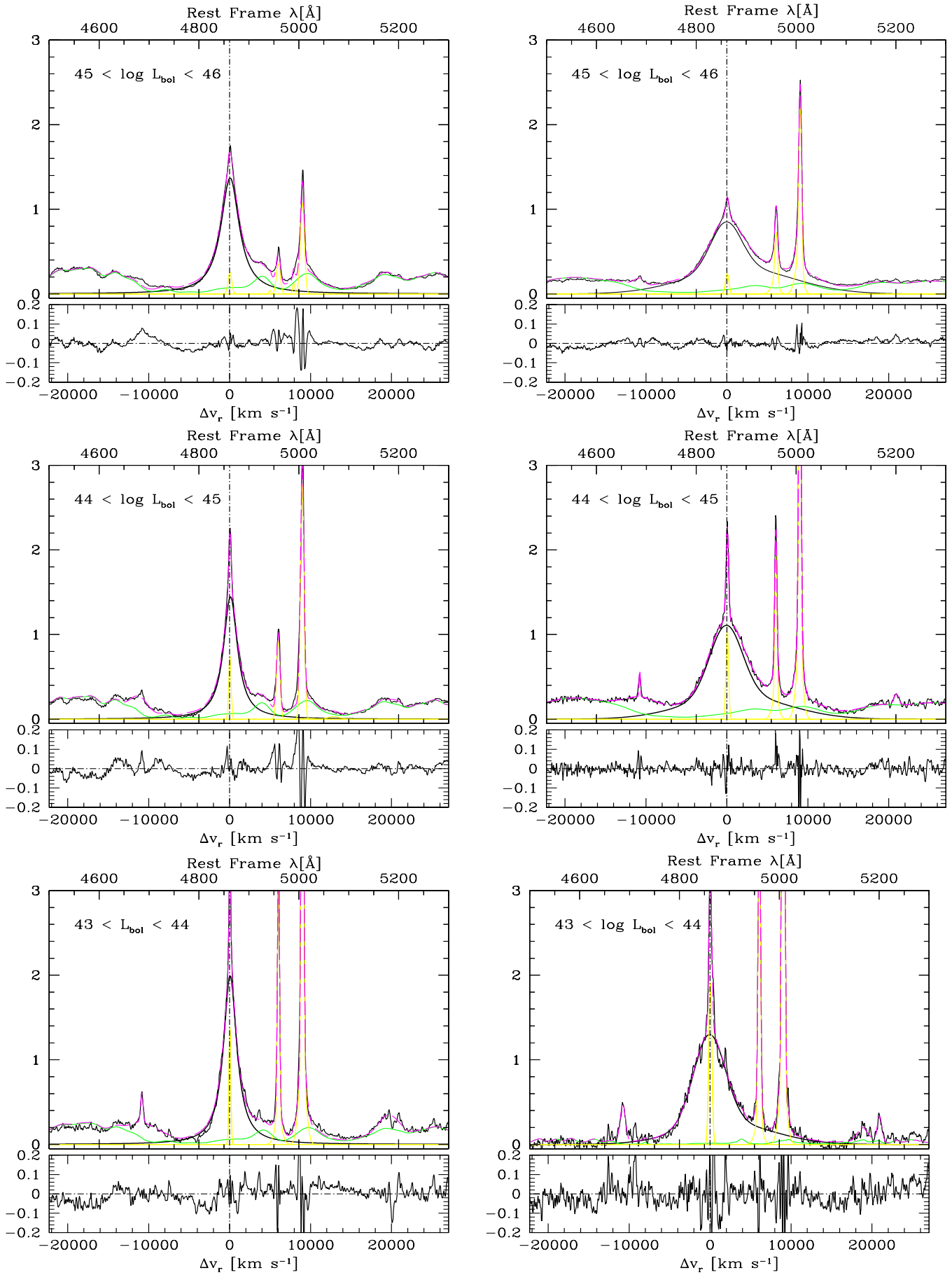
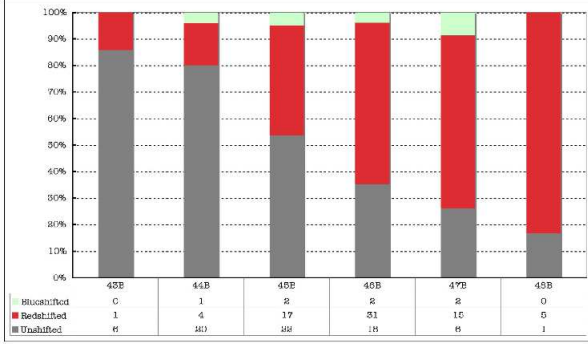
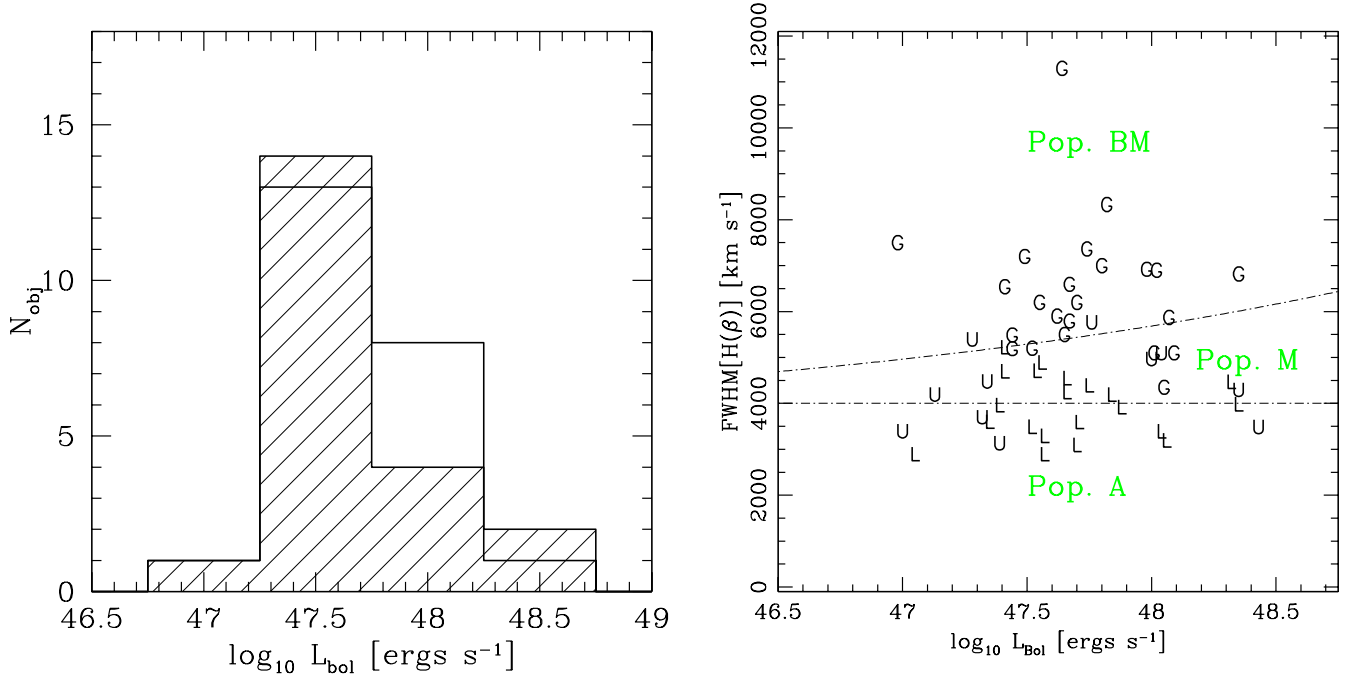


Fig. 8. Cont.





**Fig. 9.** Distribution of unshifted and shifted  $H\beta$  line centroids at 1/4 fractional intensity as a function of the bolometric luminosity ( $\log L_{\text{bol}}$ , binned over  $\Delta \log L_{\text{bol}} = 1$ , with the naming convention of Tables 6, 7, 8) for the Pop. B sources of the merged SDSS ISAAC sample. Dark grey (bottom): unshifted; grey (middle): redshifted; pale grey (top): blueshifted. “Unshifted” means that the centroid measure is 0 within a  $2\sigma$  confidence range of  $\pm 400 \text{ km s}^{-1}$ .



**Fig. 10.** Left: distribution of the ISAAC sources whose  $H\beta_{\text{BC}}$  can be fit by a Lorentzian (dashed histogram) and by a Gaussian as a function of bolometric luminosity in  $\text{ergs s}^{-1}$ . Right: the same ISAAC sources in the  $\text{FWHM}(H\beta)$  vs. bolometric luminosity plane. Each source is identified according to the best-fitting function for the core of  $H\beta$ : Lorentzian (L), Gaussian (G), or uncertain (U, undecided). The lower dot-dashed line sets the limit of Pop. A at  $4000 \text{ km s}^{-1}$ , the upper line traces the luminosity-dependent limit that may be more appropriate. In between the two lines, an intermediate population of sources (called Pop. M) show predominantly Lorentzian profiles.

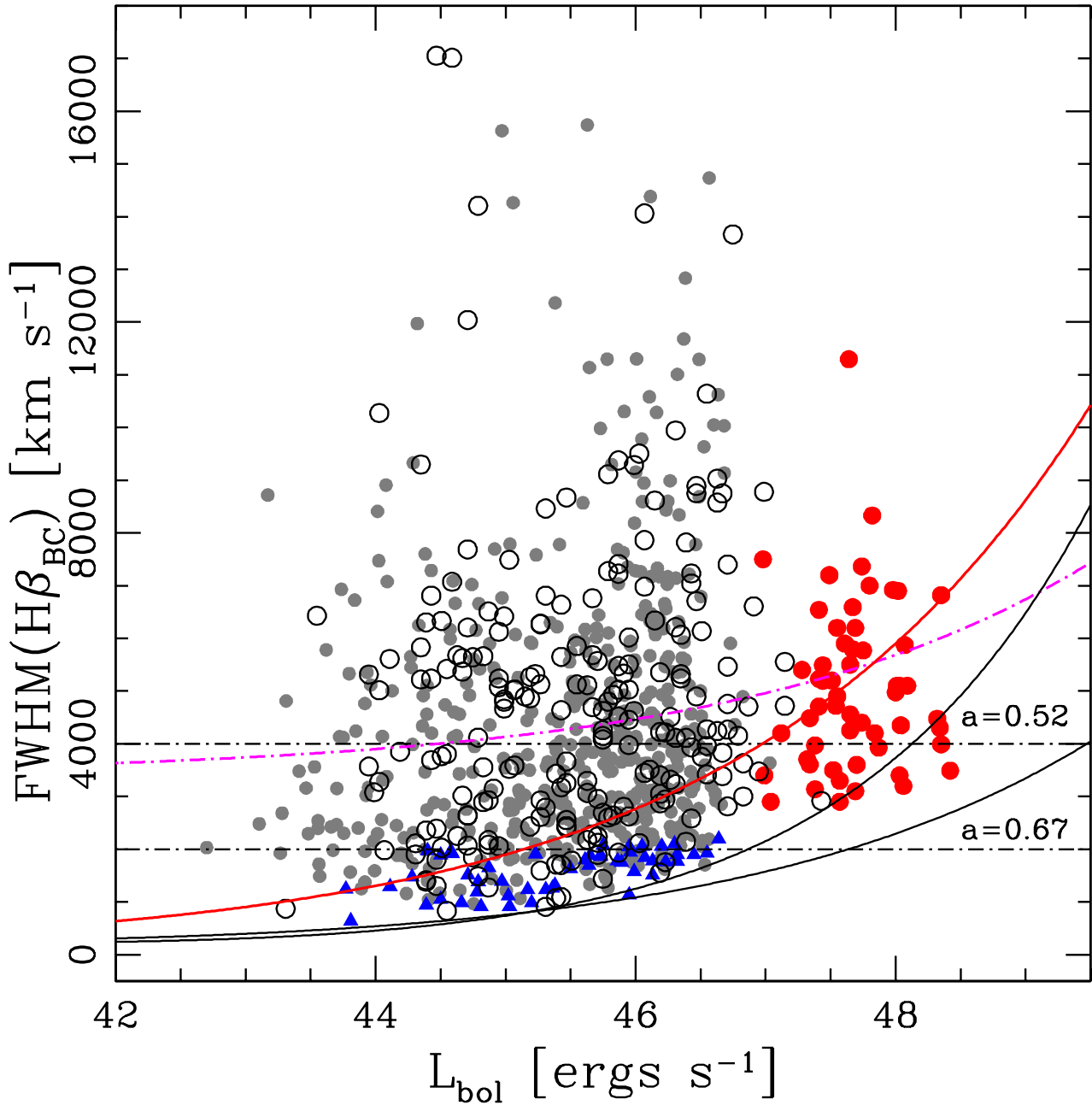


**Fig. 11.**  $\text{FWHM}(H\beta)$  in  $\text{km s}^{-1}$  as a function of bolometric luminosity. Small gray circles: data from the SDSS sample of Zamfir et al. (2008) with the “deep limit”  $g < 17.5$ ; larger filled circles: ISAAC sample; blue filled triangles: data for NLSy1s from Zhou et al. (2006). The open circles are the data points from the ATLAS of Marziani et al. (2003a). The horizontal straight, dot dashed lines show the limit of classical NLSy1s sources ( $2000 \text{ km s}^{-1}$ ) and the limit derived for Population A of Sulentic et al. (2000a) at low  $z$  i.e.,  $4000 \text{ km s}^{-1}$ . The continuous line show the minimum FWHM expected in case of virial motion, for two values of the power-law index in the relationship between BLR size and luminosity:  $a = 0.52$  (Bentz et al., 2006) and  $a = 0.67$  (Kaspi et al., 2005, Paper II). The thick dot-dashed curve at  $\text{FWHM} \approx 4000 \text{ km s}^{-1}$  traces the luminosity-dependent boundary between Pop. A and B partly adopted in this paper. The red thick lines show the FWHM increase in luminosity expected for  $L_{\text{bol}}/L_{\text{Edd}} = 0.15$  (assuming  $a = 0.67$ ).

# Online Material

**Table 1.** Basic Properties of Sources and Log of Observations

Survey name (1)	Other name (2)	$m_B^a$ (3)	$z^b$ (4)	$\Delta z^b$ (5)	Line <sup>c</sup> (6)	$M_B^d$ (7)	$\log R_K^e$ (8)	Date <sup>f</sup> (9)	Band <sup>g</sup> (10)	DIT <sup>h</sup> (11)	$N_{\text{exp}}^i$ (12)	Airmass <sup>j</sup> (13)	$S/N^k$ (14)
HE0035-2853		17.03	1.6377	0.0012	1,2,3	-28.10	< 0.21	2004/07/13	J	180	20	1.12-1.03	20
HE0043-2300		17.06	1.5402	0.0014	1	-27.89	2.03	2004/08/08	J	180	20	1.01-1.08	40
HE0058-3231	Q 0058-3231	17.14	1.5821	0.0002	1,2,3	-27.94	< 0.24	2004/07/11	J	180	20	1.02-1.01	20
HE0105-3006	Q 0105-301	16.79	1.0900	0.0004	1,3	-27.36	< 0.12	2004/07/28	sZ	180	16	1.00-1.01	10
HE0109-3518	Q 0109-3518	16.44	2.4057	0.0003	1,2,3	-29.63	< -0.04	2004/08/02	sH	180	20	1.49-1.23	20
HE0119-3325	Q 0119-3325	17.17	1.1422	0.0012	1	-27.11	1.11	2004/08/02	sZ	180	20	1.11-1.03	12
HE0142-4619		17.20	1.1665	0.0017	1	-27.12	< 0.55	2004/08/02	sZ	180	20	1.07-1.08	20
HE0142-4619								2004/08/03	J	180	20	1.62-1.34	25
HE0203-4627		17.34	1.4381	0.0007	1,2,3	-27.49	2.07	2004/08/03	J	180	20	1.28-1.15	10-15
HE0203-4627								2004/08/08	sZ	180	20	1.20-1.11	10
HE0205-3756	Q 0205-379	17.17	2.4335	0.0057	1	-28.87	1.06	2004/08/03	sH	180	32	1.05-1.03	25
HE0224-3826		16.83	1.0763	0.0012	1	-27.29	< 0.14	2004/08/04	sZ	180	16	1.06-1.03	15
HE0229-5603		17.07	1.1409	0.0015	1	-27.22	< -0.29	2004/08/18	sZ	180	16	1.52-1.36	20
HE0239-4809		17.12	1.1660	0.0009	1	-27.27	0.84	2004/08/22	sZ	180	16	1.29-1.18	20
HE0248-3628		16.58	1.5355	0.0007	1	-28.45	0.55	2004/08/22	J	180	12	1.08-1.04	25
HE0251-5550	H25.01	16.59	2.3505	0.0011	1	-29.56	< 0.23	2004/08/18	sH	180	20	1.31-1.21	35
HE0349-5249	H27.03	16.13	1.5409	...	1	-28.93	0.76	2004/08/22	J	180	12	1.17-1.14	17.5
HE0359-3959		17.09	1.5209	...	1	-27.89	0.22	2004/08/28	J	180	20	1.14-1.06	20
HE0435-4312		17.10	1.2321	0.0014	1	-27.35	< 0.51	2004/09/17	sZ	180	16	1.47-1.28	10-5
HE0436-3709		16.84	1.4447	0.0023	1	-27.93	< 0.38	2004/09/17	J	180	16	1.10-1.04	10
HE0940-1050		16.96	3.0932	...	1	-29.82	< 0.10	2005/06/10	sK	180	24	1.18-1.50	10-45
HE1039-0724		17.16	1.4584	0.0002	1,2,3	-27.86	< 0.20	2005/06/23	J	180	20	1.19-1.44	20
HE1120+0154	UM 425	16.31	1.4720	0.0004	1,2,3	-28.70	-0.57	2005/06/24	J	180	16	1.42-1.75	35
HE1347-2457		16.83	2.5986	...	1	-29.64	-0.68	2005/04/15	sH	180	28	1.16-1.54	65-10
HE1348+0118	Q 1348+0118	17.08	1.0873	0.0012	1	-27.05	< 0.24	2005/06/13	sZ	180	12	1.20-1.29	15
HE1349+0007	UM 617	16.83	1.4442	0.0010	1,2,3	-28.00	-0.18	2005/06/24	J	180	20	1.25-1.52	15
HE1409+0101		16.92	1.6497	0.0039	1	-28.30	0.40	2005/07/21	J	180	20	1.18-1.38	55-25
HE1430-0041	Q 1430-0041	16.72	1.1216	...	1	-27.60	-0.39	2005/07/21	sZ	180	16	1.43-1.78	20
HE1505+0212		17.06	1.0943	...	1	-27.28	0.51	2004/07/18	sZ	180	16	1.26-1.53	50
HE1505+0212			1.0930	0.0240	1			2005/05/21	sZ	180	20	1.28-1.57	30
HE2147-3212		16.84	1.5432	...	1	-28.15	< 0.14	2004/07/05	J	180	20	1.06-1.19	15
HE2156-4020		17.39	2.5431	0.0010	1	-28.75	-0.09	2004/07/10	sH	180	32	1.05-1.20	15-5
HE2335-3029		16.96	1.1194	0.0016	1	-27.21	< 0.20	2004/07/11	sZ	180	16	1.58-1.31	25

<sup>a</sup> Apparent B Johnson magnitude corrected because of Galactic absorption. The value of HE 0436–3709 refers to the b Strömgren magnitude.<sup>b</sup> Redshift, with uncertainty in parentheses.<sup>c</sup> Lines used for redshift calculations: 1:  $H\beta$ , 2:  $[O\text{III}]\lambda 5007$ , 3:  $[O\text{III}]\lambda 4959$ .<sup>d</sup> Absolute B magnitude, computed for  $H_0 = 70 \text{ km s}^{-1} \text{ Mpc}^{-1}$ ,  $\Omega_M = 0.3$ ,  $\Omega_\Lambda = 0.7$ , and  $k$ -correction spectral index  $a = 0.6$ .<sup>e</sup> Decimal logarithm of the specific flux ratio at 6cm and 4400 Å (effective wavelength of the B band). Upper limits are from the NVSS ( $\approx 2.5 \text{ mJy}$ ), and would place all undetected sources in the RQ domain.<sup>f</sup> Date refers to time at start of exposure.<sup>g</sup> Photometric band.<sup>h</sup> Detector Integration Time (DIT) of ISAAC, in seconds.<sup>i</sup> Number of exposures with integration time equal to DIT.<sup>j</sup> Airmass at start and end of exposure.<sup>k</sup>  $S/N$  at continuum level in the proximity of  $H\beta$ . Two values are reported in case of different  $S/N$  on the blue and red side of  $H\beta$  (blue side first). The  $S/N$  value is with  $N$  estimated at a  $2\sigma$  confidence level i.e., 2 times the rms.

**Table 2.** Measurements of Fluxes, Equivalent Widths and FWHM of Strongest Lines

Object name (1)	$F(H\beta)^a$ (2)	$W(H\beta)^b$ (3)	$F(\text{FeII}\lambda 4570)^c$ (4)	$\text{FWHM}(\text{FeII})^d$ (5)
HE0035–2853	115 <sup>+30</sup> <sub>-10</sub>	60 <sup>+17</sup> <sub>-8</sub>	101 <sup>+10</sup> <sub>-40</sub>	6400 <sup>+700</sup> <sub>-1700</sub>
HE0043–2300	214 <sup>+20</sup> <sub>-20</sub>	74 <sup>+10</sup> <sub>-10</sub>	82 <sup>+5</sup> <sub>-10</sub>	3900 <sup>+700</sup> <sub>-1300</sub>
HE0058–3231	173 <sup>+20</sup> <sub>-20</sub>	100 <sup>+15</sup> <sub>-15</sub>	60 <sup>+10</sup> <sub>-15</sub>	5800 <sup>+900</sup> <sub>-2200</sub>
HE0105–3006	58 <sup>+8</sup> <sub>-8</sub>	83 <sup>+14</sup> <sub>-14</sub>	39 <sup>+6</sup> <sub>-6</sub>	6000 <sup>+1200</sup> <sub>-2100</sub>
HE0109–3518	831 <sup>+100</sup> <sub>-100</sub>	119 <sup>+19</sup> <sub>-19</sub>	95 <sup>+20</sup> <sub>-20</sub>	...
HE0119–3325	93 <sup>+15</sup> <sub>-15</sub>	90 <sup>+17</sup> <sub>-17</sub>	64 <sup>+20</sup> <sub>-20</sub>	4500 <sup>+2000</sup> <sub>-2100</sub>
HE0142–4619	274 <sup>+30</sup> <sub>-30</sub>	133 <sup>+20</sup> <sub>-20</sub>	104 <sup>+20</sup> <sub>-40</sub>	4100 <sup>+1400</sup> <sub>-1400</sub>
HE0203–4627	159 <sup>+20</sup> <sub>-30</sub>	77 <sup>+12</sup> <sub>-16</sub>	76 <sup>+10</sup> <sub>-10</sub>	6600 <sup>+2000</sup> <sub>-1300</sub>
HE0205–3756	343 <sup>+40</sup> <sub>-15</sub>	74 <sup>+11</sup> <sub>-11</sub>	102 <sup>+10</sup> <sub>-20</sub>	4900 <sup>+1100</sup> <sub>-700</sub>
HE0224–3826	123 <sup>+15</sup> <sub>-35</sub>	77 <sup>+12</sup> <sub>-23</sub>	98 <sup>+10</sup> <sub>-20</sub> <sup>e</sup>	5100 <sup>+1800</sup> <sub>-1700</sub>
HE0229–5603	118 <sup>+10</sup> <sub>-20</sub>	77 <sup>+10</sup> <sub>-15</sub>	94 <sup>+10</sup> <sub>-10</sub>	3000 <sup>+1600</sup> <sub>-900</sub>
HE0239–4809	111 <sup>+10</sup> <sub>-10</sub>	44 <sup>+6</sup> <sub>-6</sub>	102 <sup>+20</sup> <sub>-12</sub>	2500 <sup>+1200</sup> <sub>-1200</sub>
HE0248–3628	250 <sup>+60</sup> <sub>-30</sub>	40 <sup>+10</sup> <sub>-6</sub>	119 <sup>+12</sup> <sub>-20</sub>	4300 <sup>+1100</sup> <sub>-1800</sub>
HE0251–5550	353 <sup>+40</sup> <sub>-40</sub>	71 <sup>+11</sup> <sub>-11</sub>	67 <sup>+10</sup> <sub>-25</sub>	2200 <sup>+2300</sup> <sub>-600</sub>
HE0349–5249	289 <sup>+50</sup> <sub>-50</sub>	63 <sup>+13</sup> <sub>-13</sub>	186 <sup>+20</sup> <sub>-60</sub>	4700 <sup>+600</sup> <sub>-2200</sub>
HE0359–3959	88 <sup>+15</sup> <sub>-15</sub>	45 <sup>+9</sup> <sub>-9</sub>	111 <sup>+10</sup> <sub>-24</sub>	2600 <sup>+800</sup> <sub>+1300</sub>
HE0435–4312	165 <sup>+30</sup> <sub>-30</sub>	118 <sup>+24</sup> <sub>-24</sub>	86 <sup>+10</sup> <sub>-20</sub>	5900 <sup>+1200</sup> <sub>-1800</sub>
HE0436–3709	139 <sup>+20</sup> <sub>-20</sub>	88 <sup>+15</sup> <sub>-15</sub>	78 <sup>+10</sup> <sub>-25</sub>	5200 <sup>+1900</sup> <sub>-2200</sub>
HE0940–1050	922 <sup>+200</sup> <sub>-100</sub>	43 <sup>+10</sup> <sub>-6</sub>	505 <sup>+100</sup> <sub>-100</sub> <sup>e</sup>	3000 <sup>+700</sup> <sub>-900</sub>
HE1039–0724	138 <sup>+20</sup> <sub>-20</sub>	75 <sup>+13</sup> <sub>-13</sub>	26 <sup>+5</sup> <sub>-5</sub>	...
HE1120+0154	270 <sup>+60</sup> <sub>-60</sub>	63 <sup>+15</sup> <sub>-15</sub>	35 <sup>+13</sup> <sub>-15</sub>	...
HE1347–2457	264 <sup>+20</sup> <sub>-35</sub>	64 <sup>+8</sup> <sub>-11</sub>	252 <sup>+25</sup> <sub>-60</sub>	5100 <sup>+800</sup> <sub>-1700</sub>
HE1348+0118	611 <sup>+60</sup> <sub>-60</sub>	95 <sup>+13</sup> <sub>-13</sub>	255 <sup>+55</sup> <sub>-55</sub>	4300 <sup>+600</sup> <sub>-2400</sub>
HE1349+0007	129 <sup>+20</sup> <sub>-20</sub>	76 <sup>+13</sup> <sub>+14</sub>	47 <sup>+15</sup> <sub>-10</sub>	4000 <sup>+1500</sup> <sub>-500</sub>
HE1409+0101	443 <sup>+150</sup> <sub>-100</sub>	91 <sup>+32</sup> <sub>-22</sub>	272 <sup>+20</sup> <sub>-70</sub>	6300 <sup>+2000</sup> <sub>-2100</sub>
HE1430–0041	87 <sup>+9</sup> <sub>-18</sub>	50 <sup>+7</sup> <sub>-12</sub>	78 <sup>+30</sup> <sub>-10</sub>	1000 <sup>+1000</sup> <sub>-200</sub>
HE1505+0212	176 <sup>+20</sup> <sub>-20</sub>	59 <sup>+9</sup> <sub>-9</sub>	350 <sup>+50</sup> <sub>-150</sub>	2700 <sup>+700</sup> <sub>-900</sub>
HE2147–3212	151 <sup>+20</sup> <sub>-10</sub>	82 <sup>+14</sup> <sub>-10</sub>	139 <sup>+10</sup> <sub>-40</sub>	5800 <sup>+700</sup> <sub>-1300</sub>
HE2156–4020	212 <sup>+35</sup> <sub>-20</sub>	82 <sup>+16</sup> <sub>-11</sub>	95 <sup>+15</sup> <sub>-10</sub>	5200 <sup>+1900</sup> <sub>-3000</sub>
HE2335–3029	142 <sup>+20</sup> <sub>-10</sub>	72 <sup>+12</sup> <sub>-9</sub>	25 <sup>+10</sup> <sub>-15</sub>	2000 <sup>+2000</sup> <sub>-800</sub>

<sup>a</sup> Rest frame flux of  $H\beta$  in  $\text{\AA}$   $\pm 2\sigma$  confidence level uncertainty.<sup>b</sup> Rest frame equivalent width of  $H\beta$  in  $\text{\AA}$   $\pm 2\sigma$  confidence level uncertainty.<sup>c</sup> Rest frame flux of the  $\text{FeII}\lambda 4570$  blend in units of  $\text{erg s}^{-1} \text{cm}^{-2}$ .<sup>d</sup> FWHM of lines in the blend. See text for details.<sup>e</sup> Rest frame flux of the  $\text{FeII}\lambda 4570$  blend estimated from the  $\text{FeII}\lambda 5270$  blend. See text for details.

**Table 3.** Measurements of Fluxes and Equivalent Widths of Narrow Lines

Object name (1)	$F(H\beta_{\text{NC}})^{\text{a}}$ (2)	$W(H\beta_{\text{NC}})^{\text{b}}$ (3)	$F([\text{OIII}]\lambda 5007)^{\text{c}}$ (4)	$W([\text{OIII}]\lambda 5007)^{\text{d}}$ (5)
HE0035–2853	4.0 <sup>+1.0</sup> <sub>-1.0</sub>	2.1 <sup>+0.6</sup> <sub>-0.6</sub>	12.4 <sup>+2.0</sup> <sub>-2.0</sub>	6.7 <sup>+1.2</sup> <sub>-1.2</sub>
HE0043–2300	12.0 <sup>+1.0</sup> <sub>-12.0</sub>	4.1 <sup>+0.5</sup> <sub>-1.2</sub>	27.8 <sup>+5.0</sup> <sub>-3.0</sub>	10.1 <sup>+2.0</sup> <sub>-1.5</sub>
HE0058–3231	1.8 <sup>+3.0</sup> <sub>-1.0</sub>	1.0 <sup>+1.7</sup> <sub>-0.6</sub>	13.1 <sup>+4.0</sup> <sub>-1.5</sub>	7.9 <sup>+2.4</sup> <sub>-1.2</sub>
HE0105–3006	0.3 <sup>+2.0</sup> <sub>-0.3</sub>	0.4 <sup>+2.9</sup> <sub>-0.4</sub>	1.2 <sup>+1.5</sup> <sub>-1.2</sub>	1.8 <sup>+2.2</sup> <sub>-1.7</sub>
HE0109–3518	24.4 <sup>+10.0</sup> <sub>-20.0</sub>	3.5 <sup>+1.5</sup> <sub>-1.9</sub>	247.5 <sup>+25.0</sup> <sub>-25.0</sub>	38.5 <sup>+5.3</sup> <sub>-5.3</sub>
HE0119–3325	0.8 <sup>+0.8</sup> <sub>-0.8</sub>	0.7 <sup>+1.3</sup> <sub>-0.8</sub>	1.6 <sup>+1.0</sup> <sub>-1.0</sub>	1.6 <sup>+1.5</sup> <sub>-1.0</sub>
HE0142–4619	3.9 <sup>+7.0</sup> <sub>-2.0</sub>	1.9 <sup>+3.4</sup> <sub>-1.0</sub>	20.0 <sup>+5.0</sup> <sub>-5.0</sub>	10.4 <sup>+2.6</sup> <sub>-2.6</sub>
HE0203–4627	1.0 <sup>+2.0</sup> <sub>-1.0</sub>	0.5 <sup>+1.0</sup> <sub>-0.5</sub>	8.3 <sup>+2.0</sup> <sub>-2.0</sub>	4.2 <sup>+1.1</sup> <sub>-1.1</sub>
HE0205–3756	< 7.0	< 1.5	33.0 <sup>+10.0</sup> <sub>-10.0</sub>	7.4 <sup>+2.3</sup> <sub>-2.3</sub>
HE0224–3826	1.0 <sup>+1.0</sup> <sub>-1.0</sub>	0.0 <sup>+0.6</sup> <sub>-0.6</sub>	< 3.0	< 1.9
HE0229–5603	< 1.0 <sup>±</sup>	< 0.7	4.0 <sup>+3.0</sup> <sub>-4.0</sub>	2.7 <sup>+2.0</sup> <sub>-2.6</sub>
HE0239–4809	2.8 <sup>+0.3</sup> <sub>-1.0</sub>	1.1 <sup>+0.2</sup> <sub>-0.4</sub>	7.2 <sup>+2.0</sup> <sub>-2.0</sub>	2.9 <sup>+0.8</sup> <sub>-0.8</sub>
HE0248–3628	4.8 <sup>+2.0</sup> <sub>-2.0</sub>	0.8 <sup>+0.4</sup> <sub>-0.3</sub>	15.0 <sup>+3.5</sup> <sub>-3.5</sub>	2.6 <sup>+0.6</sup> <sub>-0.6</sub>
HE0251–5550	5.6 <sup>+2.0</sup> <sub>-5.0</sub>	1.1 <sup>+0.4</sup> <sub>-1.0</sub>	49.0 <sup>+10.0</sup> <sub>-10.0</sub>	10.3 <sup>+2.2</sup> <sub>-2.2</sub>
HE0349–5249	3.3 <sup>+3.0</sup> <sub>-1.0</sub>	0.7 <sup>+0.7</sup> <sub>-0.2</sub>	11.0 <sup>+3.0</sup> <sub>-5.0</sub>	2.5 <sup>+0.7</sup> <sub>-1.1</sub>
HE0359–3959	4.3 <sup>+1.0</sup> <sub>-3.0</sub>	2.3 <sup>+0.6</sup> <sub>-2.1</sub>	0.8 <sup>+2.0</sup> <sub>-0.4</sub>	0.4 <sup>+1.0</sup> <sub>-0.2</sub>
HE0435–4312	0.4 <sup>+3.0</sup> <sub>-0.4</sub>	0.3 <sup>+2.1</sup> <sub>-0.3</sub>	13.4 <sup>+4.0</sup> <sub>-5.0</sub>	10.1 <sup>+3.0</sup> <sub>-3.7</sub>
HE0436–3709	1.5 <sup>+1.5</sup> <sub>-0.5</sub>	0.9 <sup>+1.0</sup> <sub>-0.3</sub>	3.2 <sup>+1.0</sup> <sub>-1.0</sub>	2.1 <sup>+0.7</sup> <sub>-0.7</sub>
HE0940–1050	5.5 <sup>+2.5</sup> <sub>-1.5</sub>	0.3 <sup>+0.1</sup> <sub>-0.1</sub>	11.1 <sup>+100.0</sup> <sub>-11.0</sub>	0.6 <sup>+4.7</sup> <sub>-0.5</sub>
HE1039–0724	5.0 <sup>+2.5</sup> <sub>-2.5</sub>	2.7 <sup>+1.4</sup> <sub>-1.4</sub>	26.2 <sup>+4.0</sup> <sub>-7.0</sub>	15.5 <sup>+2.7</sup> <sub>-4.1</sub>
HE1120+0154	2.2 <sup>+4.0</sup> <sub>-0.2</sub>	0.5 <sup>+0.9</sup> <sub>-0.1</sub>	52.6 <sup>+8.0</sup> <sub>-8.0</sub>	13.1 <sup>+2.3</sup> <sub>-2.3</sub>
HE1347–2457	5.0 <sup>+1.0</sup> <sub>-3.0</sub>	1.2 <sup>+0.3</sup> <sub>-0.7</sub>	< 3.0 <sup>±</sup>	5.8 <sup>+0.6</sup> <sub>-0.6</sub>
HE1348+0118	18.7 <sup>+2.0</sup> <sub>-7.0</sub>	2.9 <sup>+0.4</sup> <sub>-1.1</sub>	60.7 <sup>+10.0</sup> <sub>-20.0</sub>	10.1 <sup>+1.9</sup> <sub>-3.3</sub>
HE1349+0007	2.6 <sup>+0.5</sup> <sub>-0.5</sub>	1.5 <sup>+0.3</sup> <sub>-0.3</sub>	9.4 <sup>+2.0</sup> <sub>-2.0</sub>	6.1 <sup>+1.3</sup> <sub>-1.3</sub>
HE1409+0101	34.8 <sup>+3.0</sup> <sub>-15.0</sub>	7.1 <sup>+0.9</sup> <sub>-3.2</sub>	35.7 <sup>+5.0</sup> <sub>-10.0</sub>	7.8 <sup>+1.3</sup> <sub>-2.2</sub>
HE1430–0041	< 2.0	< 1.2	< 2.0	< 1.2
HE1505+0212	< 1.0	< 0.3	< 2.0	< 0.7
HE2147–3212	2.0 <sup>+1.0</sup> <sub>-1.0</sub>	1.1 <sup>+0.6</sup> <sub>-0.6</sub>	1.8 <sup>+1.0</sup> <sub>-1.0</sub>	1.1 <sup>+0.6</sup> <sub>-0.6</sub>
HE2156–4020	5.0 <sup>+2.0</sup> <sub>-5.0</sub>	1.9 <sup>+0.8</sup> <sub>-2.0</sub>	3.8 <sup>+1.0</sup> <sub>-3.8</sub>	1.5 <sup>+0.4</sup> <sub>-1.5</sub>
HE2335–3029	4.0 <sup>+2.0</sup> <sub>-2.0</sub>	2.0 <sup>+1.0</sup> <sub>-1.0</sub>	19.0 <sup>+4.0</sup> <sub>-2.0</sub>	10.2 <sup>+2.3</sup> <sub>-1.4</sub>

<sup>a</sup> Rest frame flux of  $H\beta_{\text{NC}}$  in units of  $10^{-15}$  erg  $\text{s}^{-1}$   $\text{cm}^{-2}$ .

<sup>b</sup> Rest frame equivalent width of  $H\beta_{\text{NC}}$  in  $\text{\AA}$ .

<sup>c</sup> Rest frame flux of  $[\text{OIII}]\lambda 5007$  in units of  $10^{-15}$  erg  $\text{s}^{-1}$   $\text{cm}^{-2}$ .

<sup>d</sup> Rest frame equivalent width of the  $[\text{OIII}]\lambda 5007$  line in  $\text{\AA}$ .

**Table 4.** H $\beta$  Line Profile Measurements

Source (1)	FWZI <sup>a</sup> (2)	$\Delta^{a,b}$ (3)	FWHM <sup>a</sup> (4)	$\Delta^{a,b}$ (5)	A.I. <sup>c</sup> (6)	$\Delta^b$ (7)	Kurt. <sup>d</sup> (8)	$\Delta^b$ (9)
HE0035-2853	23300	3600	7400	500	0.19	0.07	0.37	0.04
HE0043-2300	25000	4500	4600	300	-0.03	0.10	0.33	0.06
HE0058-3231	25200	4400	5800	500	0.22	0.08	0.30	0.04
HE0105-3006	20700	5000	5200	400	0.10	0.17	0.28	0.08
HE0109-3518	24400	5900	4000	300	-0.01	0.10	0.33	0.06
HE0119-3325	25300	6800	4500	300	0.03	0.09	0.41	0.06
HE0142-4619	26900	4200	3600	300	0.24	0.17	0.26	0.08
HE0203-4627	27800	5100	7200	500	0.12	0.09	0.32	0.05
HE0205-3756	20700	4400	4400	400	0.41	0.06	0.16	0.03
HE0224-3826	20800	2900	6500	400	0.10	0.07	0.40	0.05
HE0229-5603	26500	6300	4000	300	0.03	0.10	0.31	0.06
HE0239-4809	19700	3900	4700	400	0.19	0.14	0.27	0.06
HE0248-3628	22200	4400	3900	300	-0.19	0.10	0.30	0.05
HE0251-5550	25700	4400	4500	400	0.47	0.07	0.19	0.03
HE0349-5249	26500	4000	5900	800	0.37	0.07	0.27	0.04
HE0359-3959	18500	4800	4300	400	-0.15	0.09	0.30	0.05
HE0435-4312	25300	6100	5500	300	0.08	0.14	0.38	0.08
HE0436-3709	26700	4300	6600	500	0.26	0.09	0.32	0.05
HE0940-1050	15400	1400	3500	200	0.53	0.04	0.22	0.02
HE1039-0724	22900	3300	11300	500	0.63	0.04	0.48	0.03
HE1120+0154	25800	4300	6900	500	0.33	0.07	0.35	0.04
HE1347-2457	24700	3600	6800	500	0.20	0.09	0.31	0.05
HE1348+0118	23600	4400	3700	200	0.08	0.15	0.38	0.08
HE1349+0007	23400	3500	6200	400	0.27	0.10	0.34	0.06
HE1409+0101	21600	4600	8300	900	0.48	0.07	0.28	0.03
HE1430-0041	19100	3600	4700	300	-0.05	0.10	0.33	0.06
HE1505+0212	18400	2300	5200	200	-0.02	0.25	0.37	0.11
HE2147-3212	25900	3900	5800	400	0.01	0.10	0.33	0.05
HE2156-4020	26200	4400	5000	500	0.27	0.10	0.26	0.05
HE2335-3029	18100	4000	3100	200	0.04	0.11	0.38	0.07

<sup>a</sup> In units of km s<sup>-1</sup>.<sup>b</sup> 2 $\sigma$  confidence level uncertainty.<sup>c</sup> Asymmetry index defined as in Marziani et al. (1996).<sup>d</sup> Kurtosis parameter as in Marziani et al. (1996).

**Table 5.**  $H\beta$  Line Centroids at Different Fractional Heights

Source (1)	$c(0/4)^a$ (2)	$\Delta^{a,b}$ (3)	$c(1/4)^a$ (4)	$\Delta^{a,b}$ (5)	$c(1/2)^a$ (6)	$\Delta^{a,b}$ (7)	$c(3/4)^a$ (8)	$\Delta^{a,b}$ (9)	$c(0.9)^a$ (10)	$\Delta^{a,b}$ (11)
HE0035-2853	3100	1800	1900	400	930	270	490	200	370	130
HE0043-2300	100	2200	100	400	130	160	130	120	130	80
HE0058-3231	3500	2200	2500	500	1010	240	710	150	640	100
HE0105-3006	2900	2500	1000	1000	290	180	250	140	240	90
HE0109-3518	400	3000	0	300	40	140	40	110	40	70
HE0119-3325	800	3400	100	300	40	130	30	120	20	80
HE0142-4619	1300	3400	100	300	40	130	30	120	20	80
HE0203-4627	-300	2100	1000	800	200	150	110	100	90	60
HE0205-3756	2900	2200	2600	500	580	220	80	110	10	60
HE0224-3826	3400	1500	1100	400	650	200	400	180	300	120
HE0229-5603	1500	3200	-100	300	-110	150	-110	110	-110	60
HE0239-4809	-100	2000	200	600	-330	180	-330	130	-310	70
HE0248-3628	500	2200	-400	400	10	160	130	110	150	60
HE0251-5550	2900	2200	2900	600	90	200	-60	120	-90	70
HE0349-5249	2700	2000	2200	500	640	420	100	150	20	90
HE0359-3959	-700	2400	-800	400	-320	180	-140	120	-90	70
HE0435-4312	2700	3100	400	600	100	160	50	150	40	100
HE0436-3709	2600	2100	2100	600	570	240	310	180	240	120
HE0940-1050	3200	700	2700	200	0	90	0	90	0	70
HE1039-0724	2000	1600	1900	300	1270	250	140	830	-1380	160
HE1120+0154	2700	2200	1300	500	60	260	-260	190	-350	120
HE1347-2457	2400	1800	0	600	-390	270	-570	190	-610	110
HE1348+0118	3400	2200	300	400	70	110	30	100	30	70
HE1349+0007	3000	1700	1400	700	180	200	-10	170	-60	110
HE1409+0101	800	2300	1600	500	510	460	-700	210	-860	110
HE1430-0041	-400	1800	200	400	200	170	200	130	200	80
HE1505+0212	-800	1200	0	900	-390	110	-60	260	30	80
HE2147-3212	-1300	2000	-100	500	-70	210	-70	160	-70	100
HE2156-4020	1700	2200	1600	500	390	250	150	130	100	80
HE2335-3029	800	2000	100	300	10	90	-10	80	-10	60

<sup>a</sup> In units of  $\text{km s}^{-1}$ .<sup>b</sup>  $2\sigma$  confidence level uncertainty.



**Table 6.** Measurements on the Broad Lines of Median Spectra

Object name (1)	W(H $\beta$ ) <sup>a</sup> (2)	W(FeII $\lambda$ 4570) <sup>a</sup> (3)	FWHM(FeII) <sup>b</sup> (4)	F(H $\beta_{BC}$ )/F(H $\beta$ ) <sup>c</sup> (5)	FWHM(H $\beta_{BC}$ ) <sup>d</sup> (6)	log $M_{BH}$ H $\beta_{BC}$ <sup>e</sup> (7)	log $L_{bol}/L_{Edd}$ H $\beta_{BC}$ <sup>e</sup> (8)
A1	72 <sup>+11</sup> <sub>-11</sub>	26 <sup>+3</sup> <sub>-4</sub>	2700 <sup>+1100</sup> <sub>-1100</sub>	1.00	...	...	...
A2	65 <sup>+10</sup> <sub>-10</sub>	49 <sup>+13</sup> <sub>-11</sub>	3700 <sup>+2000</sup> <sub>-1400</sub>	1.00	...	...	...
B1	86 <sup>+13</sup> <sub>-13</sub>	26 <sup>+5</sup> <sub>-6</sub>	5200 <sup>+1400</sup> <sub>-2300</sub>	0.27	4000	...	...
B2	70 <sup>+11</sup> <sub>-11</sub>	44 <sup>+8</sup> <sub>-14</sub>	5000 <sup>+800</sup> <sub>-1700</sub>	0.32	4000	...	...
A	61 <sup>+10</sup> <sub>-13</sub>	25 <sup>+7</sup> <sub>-7</sub>	2700 <sup>+1500</sup> <sub>-1200</sub>	1.00	...	...	...
M	67 <sup>+10</sup> <sub>-11</sub>	35 <sup>+7</sup> <sub>-6</sub>	3800 <sup>+1450</sup> <sub>-1200</sub>	1.00	...	...	...
MB	86 <sup>+10</sup> <sub>-13</sub>	31 <sup>+6</sup> <sub>-7</sub>	5000 <sup>+1600</sup> <sub>-1800</sub>	0.27	4100	...	...
43A	91 <sup>+10</sup> <sub>-20</sub>	36 <sup>+7</sup> <sub>-7</sub>	3000 <sup>+500</sup> <sub>-750</sub>	1.00	...	6.1	-0.74
44A	69 <sup>+15</sup> <sub>-15</sub>	38 <sup>+10</sup> <sub>-10</sub>	2600 <sup>+500</sup> <sub>-750</sub>	1.00	...	6.8	-0.47
45A	86 <sup>+10</sup> <sub>-10</sub>	43 <sup>+10</sup> <sub>-10</sub>	2800 <sup>+750</sup> <sub>-500</sub>	1.00	...	7.8	-0.43
46A	80 <sup>+10</sup> <sub>-10</sub>	47 <sup>+10</sup> <sub>-10</sub>	3000 <sup>+600</sup> <sub>-600</sub>	1.00	...	8.6	-0.26
47A	68 <sup>+10</sup> <sub>-11</sub>	30 <sup>+8</sup> <sub>-8</sub>	3000 <sup>+1400</sup> <sub>-1200</sub>	1.00	...	9.6	-0.20
48A	60 <sup>+11</sup> <sub>-11</sub>	27 <sup>+5</sup> <sub>-8</sub>	3800 <sup>+1500</sup> <sub>-1100</sub>	1.00	...	10.3	+0.11
43B	130 <sup>+20</sup> <sub>-20</sub>	8 <sup>+10</sup> <sub>-7</sub>	... <sup>f</sup>	0.59	4600	7.1	-0.68
44B	125 <sup>+10</sup> <sub>-30</sub>	38 <sup>+5</sup> <sub>-20</sub>	5600 <sup>+600</sup> <sub>-1800</sub>	0.49	4700	7.7	-1.37
45B	111 <sup>+15</sup> <sub>-20</sub>	29 <sup>+5</sup> <sub>-15</sub>	4900 <sup>+500</sup> <sub>-800</sub>	0.35	4400	8.4	-0.98
46B	93 <sup>+10</sup> <sub>-20</sub>	22 <sup>+5</sup> <sub>-10</sub>	5900 <sup>+350</sup> <sub>-1200</sub>	0.37	4800	9.1	-0.73
47B	92 <sup>+13</sup> <sub>-14</sub>	38 <sup>+7</sup> <sub>-7</sub>	4900 <sup>+1600</sup> <sub>-2000</sub>	0.27	4000	9.6	-0.24
48B	75 <sup>+9</sup> <sub>-11</sub>	12 <sup>+3</sup> <sub>-3</sub>	4600 <sup>+1200</sup> <sub>-1700</sub>	0.23	4300	10.3	+0.03

<sup>a</sup> Equivalent width of H $\beta$  (H $\beta_{BC}$ + H $\beta_{VBC}$ ) and FeII $\lambda$ 4570 in  $\text{\AA}$   $\pm 2\sigma$  confidence level uncertainty. Note that those values have been computed on median spectra with flux normalized to unity at  $\lambda = 5100 \text{ \AA}$ . Considering that the continuum shape is not flat, but that there is however little dispersion in continuum shape across the median spectra, it is  $W(H\beta) \approx I(H\beta)/1.1$ , and  $W(FeII\lambda 4570) \approx I(FeII\lambda 4570)/1.25 \text{ \AA}$ .

<sup>b</sup> FWHM of lines in the blend in units of  $\text{km s}^{-1}$  computed by `specfit` as for the individual sources. Uncertainty is at  $\pm 2\sigma$  confidence level. See text for details.

<sup>c</sup> Intensity ratio of the H $\beta_{BC}$  to total H $\beta$  line emission i.e., H $\beta_{BC}$  and H $\beta_{VBC}$ .

<sup>d</sup> FWHM of the H $\beta_{BC}$  component i.e., after removing H $\beta_{VBC}$ .

<sup>e</sup> Logarithm of  $M_{BH}$ , in solar masses, and of  $L_{bol}/L_{Edd}$ . Values have been computed following Paper II, using the FWHM(H $\beta_{BC}$ ) reported in Col. (6), and assuming the average bin luminosity. Values are therefore only indicative. No  $M_{BH}$  or  $L_{bol}/L_{Edd}$  has been computed for median in spectral types since they are normalized median spectra made regardless of their luminosity.

<sup>f</sup> FeII<sub>opt</sub> too faint for FWHM to be meaningfully constrained.

**Table 7.**  $H\beta$  Line Profile Measurements on Spectral Types

Source (1)	FWZI <sup>a</sup> (2)	$\Delta^{a,b}$ (3)	FWHM <sup>a</sup> (4)	$\Delta^{a,b}$ (5)	A.I. <sup>c</sup> (6)	$\Delta^b$ (7)	Kurt. <sup>d</sup> (8)	$\Delta^b$ (9)
A1	35000	14000	3500	300	0.01	0.10	0.33	0.06
A2	41100	16000	4100	300	0.05	0.10	0.33	0.06
B1	34700	6000	5900	600	0.37	0.10	0.25	0.04
B2	29200	5000	5700	500	0.26	0.09	0.29	0.05
A	37100	15000	3700	300	0.02	0.10	0.33	0.06
M	43700	17000	4400	300	0.01	0.10	0.33	0.06
BM	34400	6000	6300	700	0.35	0.09	0.25	0.04
43A	19800	8000	2000	100	-0.05	0.11	0.33	0.07
44A	20700	8000	2100	100	-0.07	0.11	0.33	0.07
45A	27300	11000	2700	200	-0.01	0.10	0.33	0.06
46A	31000	12000	3100	200	-0.04	0.10	0.33	0.06
47A	40000	16000	4000	300	0.01	0.10	0.33	0.06
48A	40900	16000	4100	300	0.05	0.10	0.33	0.06
43B	27900	6400	5200	300	0.06	0.09	0.41	0.05
44B	31600	6600	5700	300	0.07	0.11	0.39	0.06
45B	34800	6400	6000	400	0.20	0.13	0.30	0.06
46B	32900	5900	6500	500	0.22	0.10	0.31	0.05
47B	36900	6400	5900	500	0.29	0.11	0.25	0.05
48B	29400	4600	9300	900	0.44	0.06	0.29	0.03

<sup>a</sup> In units of  $\text{km s}^{-1}$ .<sup>b</sup>  $2\sigma$  confidence level uncertainty.<sup>c</sup> Asymmetry index defined as in Marziani et al. (1996).<sup>d</sup> Kurtosis parameter as in Marziani et al. (1996).**Table 8.**  $H\beta$  Line Centroids at Different Fractional Heights on Spectral Types

Source (1)	$c(0/4)^a$ (2)	$\Delta^{a,b}$ (3)	$c(1/4)^a$ (4)	$\Delta^{a,b}$ (5)	$c(1/2)^a$ (6)	$\Delta^{a,b}$ (7)	$c(3/4)^a$ (8)	$\Delta^{a,b}$ (9)	$c(0.9)^a$ (10)	$\Delta^{a,b}$ (11)
A1	0	6900	0	300	-30	130	-30	100	-30	60
A2	-100	8200	-200	300	-170	150	-170	110	-170	70
B1	2400	3000	2100	700	130	280	-130	150	-170	100
B2	2200	2600	1700	600	380	230	170	150	130	100
A	-100	7400	-100	300	-70	130	-70	100	-70	60
M	0	8700	0	400	-40	160	-40	120	-40	70
BM	2400	2900	2200	700	270	330	-60	160	-120	100
43A	100	3900	100	200	90	70	90	50	90	30
44A	200	4100	100	200	130	70	130	60	130	40
45A	0	5400	0	200	30	100	30	80	30	50
46A	100	6200	100	300	120	110	120	90	110	50
47A	0	7900	0	300	-20	140	-20	110	-20	70
48A	-100	8100	-200	300	-170	150	-170	110	-170	70
43B	2100	3200	200	300	40	150	0	140	-10	100
44B	1200	3300	200	500	10	170	-30	150	-40	100
45B	1700	3200	1200	800	140	210	40	160	20	100
46B	2400	3000	1600	700	370	230	190	170	150	110
47B	2100	3200	2000	800	220	260	30	160	0	100
48B	3100	2300	2700	400	1550	440	-20	240	-230	120

<sup>a</sup> In units of  $\text{km s}^{-1}$ .<sup>b</sup>  $2\sigma$  confidence level uncertainty.

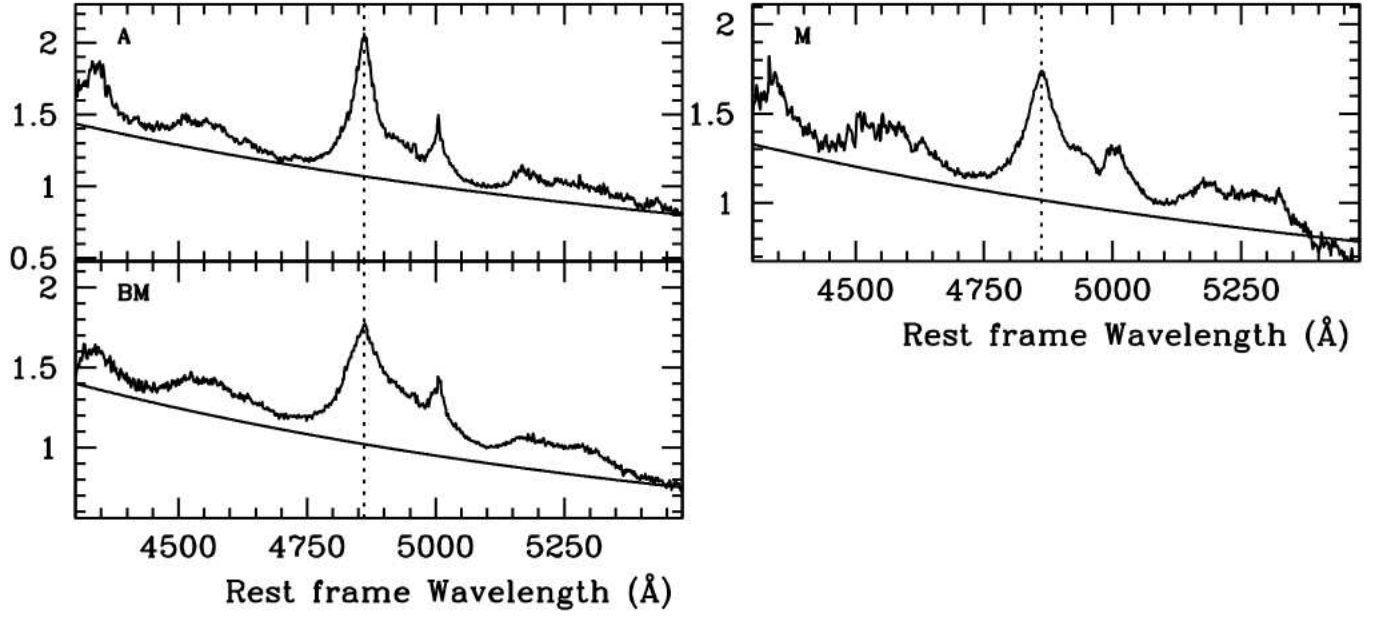


**Fig. 12.** Median spectra for Population A, intermediate spectra in region M, and modified Population B (BM), as defined in Fig. 10.

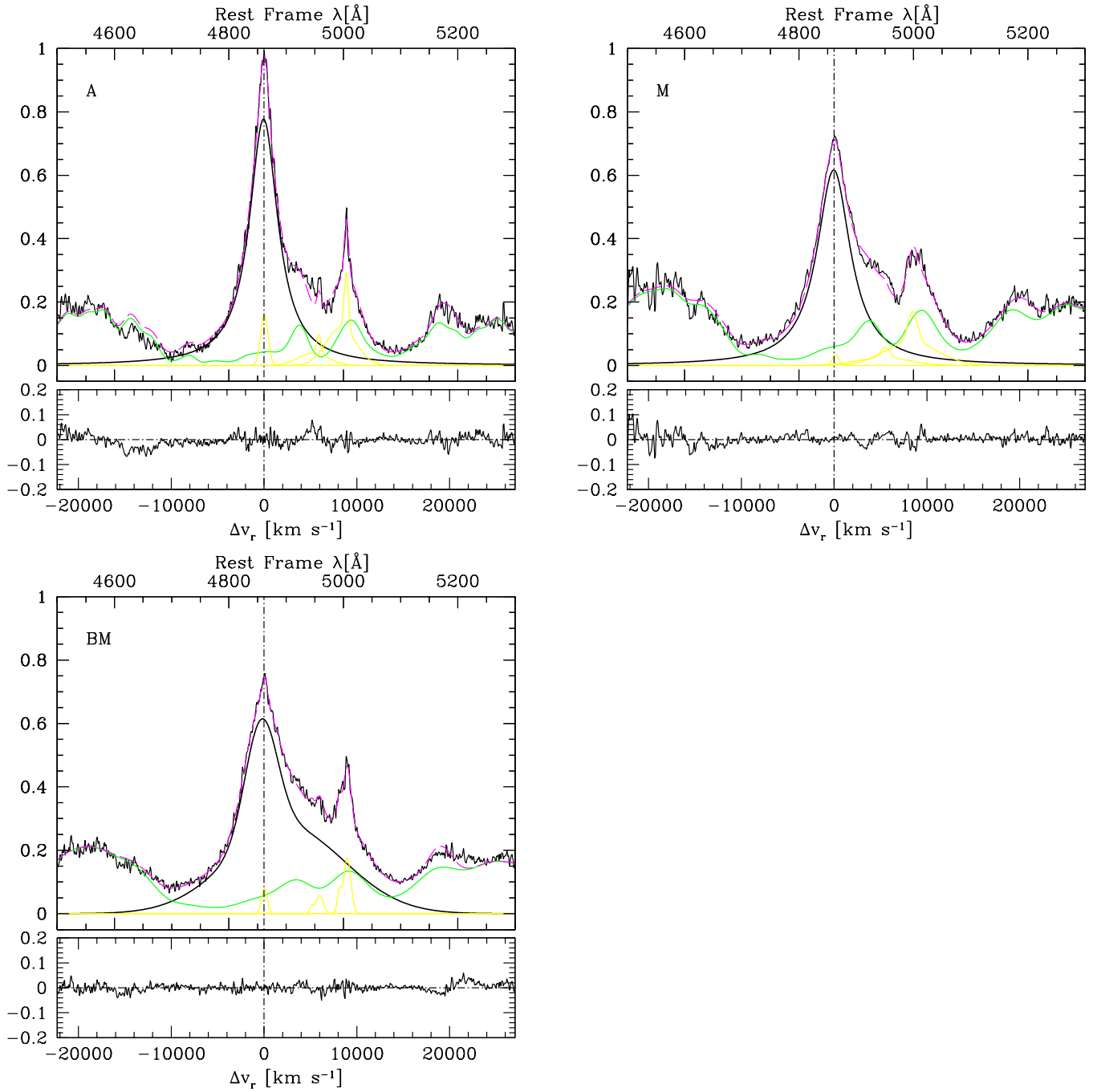


**Fig. 13.** Median spectra analysis of the  $H\beta$  profiles for Population A, “middle” Population M, and Population MB. Units and line formats are the same as for Fig. 8.

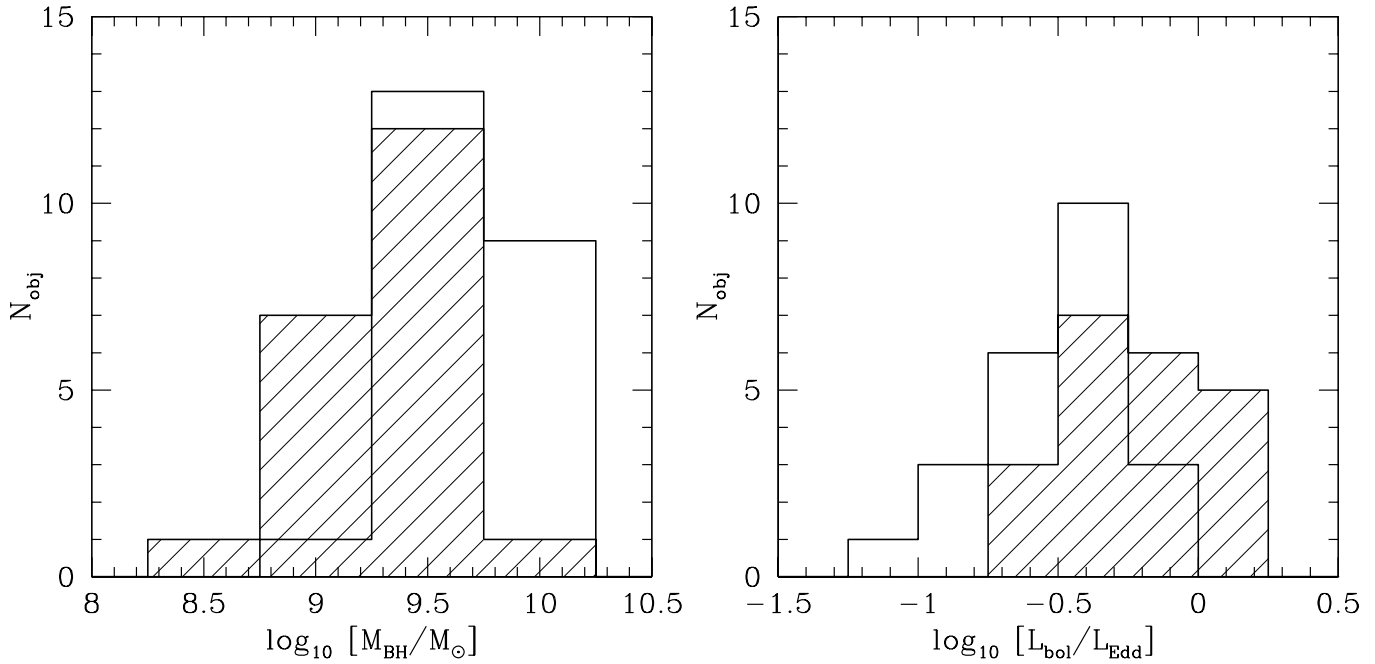


**Fig. 14.** Distribution of sources whose  $H\beta_{BC}$  is of Lorentzian (hatched histogram) or Gaussian type as a function of black hole mass in units of solar masses (left) and of Eddington ratio (right).

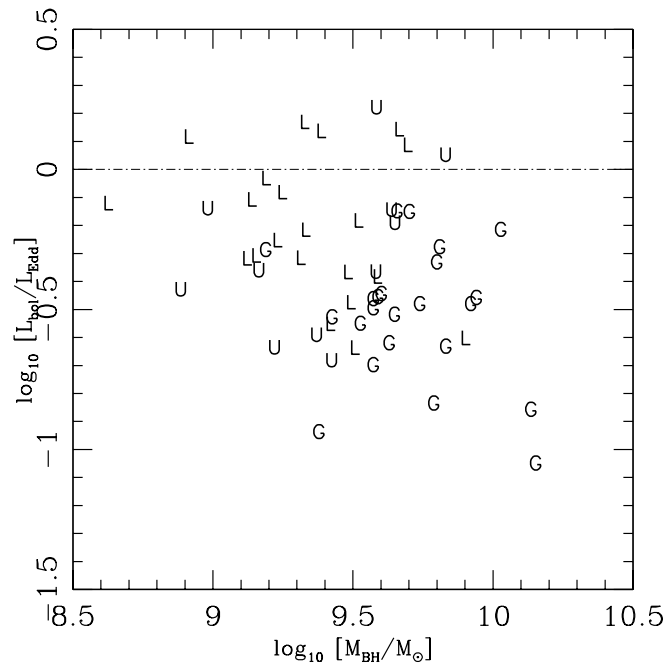


**Fig. 15.** Distribution of the ISAAC sources in the  $L_{bol}/L_{Edd}$  vs.  $M_{BH}$  (in solar units) plane. Each source is labeled as in Fig. 10.

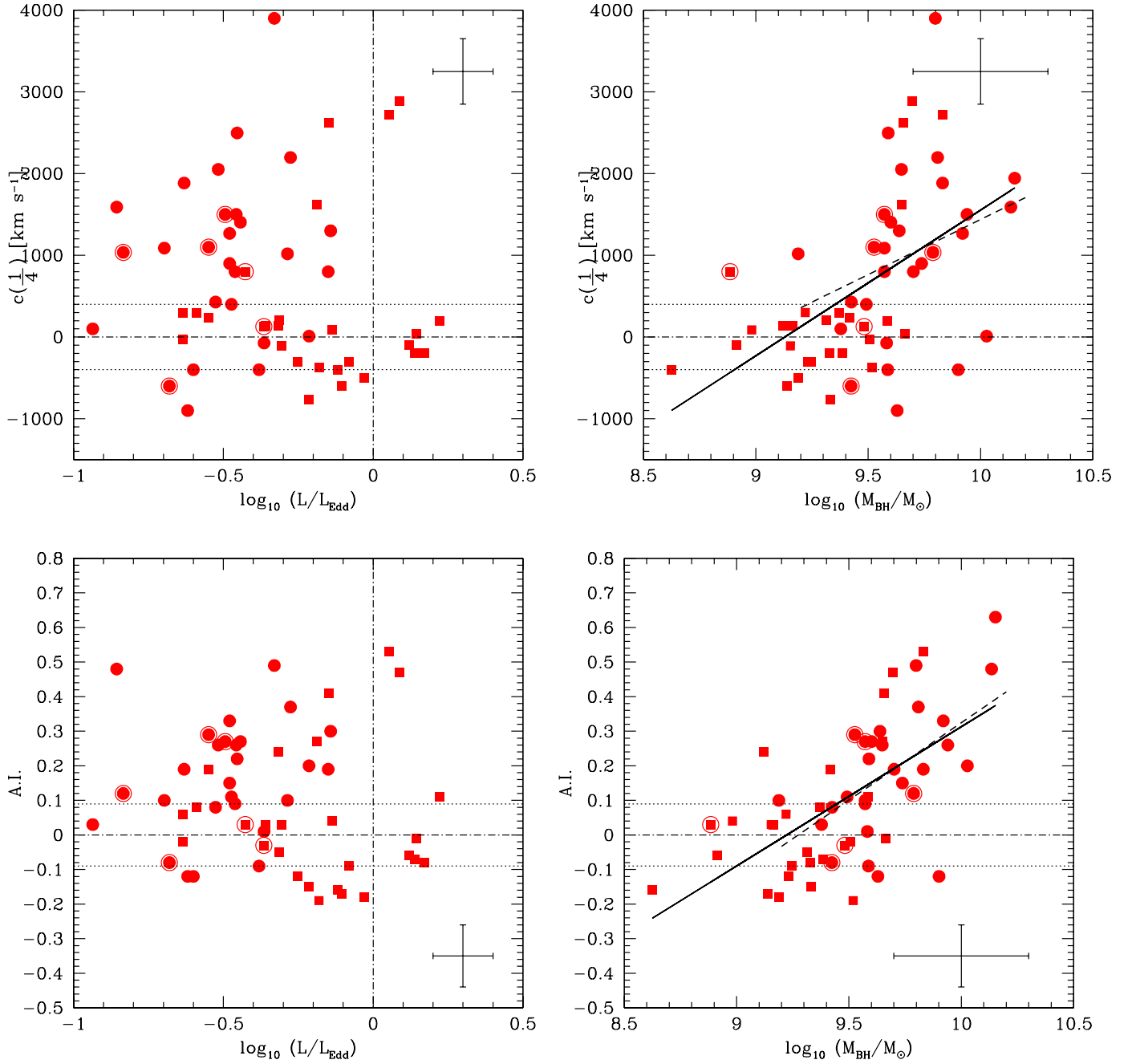


**Fig. 16.** Dependence on black hole  $M_{\text{BH}}$  and Eddington ratio for H $\beta$   $c(\frac{1}{4})$  (upper panels) and A.I. (lower panels).  $c(\frac{1}{4})$  is in units of  $\text{km s}^{-1}$ ,  $M_{\text{BH}}$  in units of solar masses. Circled data points identify RL sources. Typical error bars at a  $2\sigma$  confidence levels are displayed in the corners of each panel. Significant correlations are presents for  $c(\frac{1}{4})$  and A.I. vs.  $\log M_{\text{BH}}$ ; the thick lines are best fits with the unweighted least squares method. The dashed lines represent unweighted least squares fits restricted to Pop. B.

